Hindawi
International Journal of Energy Research
Volume 2023, Article ID 3849631, 22 pages
https://doi.org/10.1155/2023/3849631

Research Article

Mobile Proton-Exchange Membrane Fuel Cell Powered by Diesel Fuel: System Simulation and Life Cycle Analysis

Hyewon Hwang,[1] **Jisu Yoon**,[1] **and Wonjae Choi**[1,2]

[1]*Division of Mechanical and Biomedical Engineering, Ewha Womans University, 52 Ewhayeodae-gil, Seodaemun-gu, Seoul 03760, Republic of Korea*
[2]*Graduate Program in System Health Science and Engineering, Ewha Womans University, 52 Ewhayeodae-gil, Seodaemun-gu, Seoul 03760, Republic of Korea*

Correspondence should be addressed to Wonjae Choi; wj_choi@ewha.ac.kr

Received 20 May 2023; Revised 20 September 2023; Accepted 25 September 2023; Published 12 October 2023

Academic Editor: Debabrata Barik

Diesel engine generators used at construction sites generate noise, vibration, and large amounts of pollutant emissions. With the strengthening of emission standards for construction equipment, technologies must be developed to meet new requirements. We proposed and analyzed a mobile proton-exchange membrane fuel cell diesel-powered system to address these issues. The proposed system consisted of an autothermal reformer, a proton-exchange membrane fuel cell, and a balance of plant components. Previous studies on the system have not explored the optimal design and operating condition of the system and have not shown whether the proposed system is superior to the system using the hydrogen-fueled proton-exchange membrane fuel cell system in the life-cycle greenhouse gas emissions point of view. In this study, we clarified system operation characteristics, determined the operational design point, and evaluated system performance and life-cycle greenhouse gas emissions. The system was analyzed by constructing a zero-dimensional simulation model. Several control parameters were varied in parametric studies to determine the operational design point (steam-to-carbon ratio of 2, oxygen-to-carbon ratio of 0.5, fuel utilization factor of 0.85, and heat exchanger effectiveness of 0.85). Considering system performance, the determined design point achieved a 32.3% efficiency. Additionally, we assessed the life-cycle greenhouse gas emissions of the system and compared them with those of an alternative system, which is a hydrogen-fueled proton exchange membrane fuel cell system. It was confirmed that in the United States of America, the proposed system emits 1010.2 g-$CO_{2\text{-eq}}$/kWh of greenhouse gas at a 300 km fuel transportation distance, which is similar to a hydrogen-fueled proton-exchange membrane fuel cell system (1001.1 g-$CO_{2\text{-eq}}$/kWh). The proposed system emits less greenhouse gas emissions than the hydrogen-fueled proton-exchange membrane fuel cell system if the distance from the hydrogen production site to the construction site is more than 318 km. Therefore, for a construction site far from a hydrogen production plant, the proposed diesel-fueled proton-exchange membrane fuel cell system is preferable from both the greenhouse gas emissions and convenience perspectives.

1. Introduction

With the escalating climate crisis severity, the international community's goal is net zero carbon emissions by 2050. As a core societal component, the construction industry is responsible for disaster recovery, social overhead capital such as roads and railroads, public building assembly, and public facility expansion. Engine-type generators are mainly used at construction sites to power various construction machines, such as handheld breakers, air compressors, and welding instruments. The electric energy required for construction work in mountains, fields, or disaster recovery areas is typically supplied through mobile engine generators. Although diesel-engine generators have low investment costs, they emit considerable greenhouse gas (GHG) and pollutant emissions such as nitrogen oxides (NOx), sulfur oxides (SOx), and fine dust.

Construction equipment emission standards in the United States (U.S.) and Europe are gradually strengthened

to reduce emission levels. Europe announced Stage V standards for regulating particulate matter (PM) levels in April 2017, which involved approximately 97% stricter regulations for PM and 94% stricter for hydrocarbon (HC) and NOx compared to those in stage I [1]. The Environment Protection Agency prepares vehicle and engine emission standards in the United States. Tier-4 Final regulations apply to nonroad engines, strengthening NOx and PM regulations and requiring an after-treatment system [2]. Moreover, the California Air Resources Board held its first public workshop on Tier-5 regulations in November 2021 [3]. In addition, the Clean Air Conservation Act of Korea has been incorporated based on the US Tier-4-Final construction and agricultural machinery regulations since 2015 [4]. Considering these aspects, diesel-powered generator adherence to these new emission standards is essential; thus, various researches has been performed, such as using alternative diesel fuels and developing a new diesel-powered system [5].

Developing a new diesel-powered system not based on an internal combustion engine has gained attention because diesel engine generators are classified as declarable noise-generating equipment at construction sites [6]. Therefore, the considerable noise from generator use must also be diminished in addition to emission levels. According to the National Environmental Dispute Resolution Commission of the Ministry of Environment in Korea, from 1991 to 2017, 3,241 out of 3,819 environmental disputes were related to construction and road noise and vibration levels [7].

Fuel cells are power generators that produce heat and electricity from the electrochemical reaction of hydrogen (H_2) and oxygen (O_2). Since this process does not involve combustion, such fuel cells do not emit pollutant emissions, and installation locations are unlimited [8]. Therefore, fuel cell technologies represent a promising technology to alleviate the environmental and noise problems associated with construction equipment [9]. Especially the proton-exchange membrane fuel cell (PEMFC) is the type that has the advantages of high-power density, quiet operation, high efficiency, and quick start-up [10]. Many studies improve the efficiency of the fuel cell by optimizing flow-field design not only materials [11, 12].

There are few construction cases involving hydrogen fuel cell generators [13]. For example, French start-up EODev developed the GEH_2 Hydrogen Genset for isolated areas, construction sites, and events. It produces 110 kW of power [14]. GeoPura and Siemens Energy applied hydrogen fuel cell generators to the National Grid's Viking Link construction site [15]. Hydrogen was produced from steam methane reforming (SMR) and electrolysis, transported to the construction site, and supplied to fuel cell generators [16].

However, diesel's hydrogen storage density is more than two times that of liquid hydrogen, and because it is easy to store and transport, it is suitable for mobile generator use. In addition, diesel production and supply systems are well-equipped compared to H_2. Therefore, through diesel-powered fuel cells' successful technological development, fuel cells can be applied in construction sites, accelerating market expansion.

Considering these aspects, many research groups focus on diesel reformers for fuel cell-based auxiliary power units (APUs). The primary challenge in using diesel fuel lies in its high carbon content, which can lead to carbon deposition on the fuel cell's catalyst. For example, Rosa et al. designed a 5 kW diesel fuel processor for an integrated operation with a PEMFC. Their proposed prototype achieved less than 100 ppm carbon monoxide (CO) concentration in the gas after using the preferential oxidizer (PROX) [17]. Krummrich et al. substantiated the feasibility of reforming F76 diesel fuel with steam for PEMFC. The fuel processor unit had an 82% overall efficiency at full load [18]. Lindstrom et al. proposed a commercial diesel-fueled power generation system by integrating a PEMFC and an autothermal reformer (ATR). Their study identified critical factors for achieving a high reforming efficiency and low diesel slip through computational reformer fluid dynamics calculations. It demonstrated that a diesel reforming conversion efficiency of up to 83% could be achieved [19]. Song et al. analyzed three different reforming methods (autothermal reforming, partial oxidation, and steam reforming) by means of thermodynamic analysis. They showed that the petrol autothermal reforming system had the largest ideal thermal efficiency of 91.22%, whereas the steam reforming (SR) system was 89.57% [20]. Ješić et al. simulated the auto-thermal reforming with the operational water-gas shift (WGS) using Aspen Plus. They analyzed the influence of the oxygen-to-carbon ratio, steam-to-carbon ratio, inlet ATR temperature, and pressure [21]. Lee et al. suggested diesel fuel processing utilizing hydrogen peroxide (H_2O_2) to obtain the high-purity H_2. They achieved 65.8% efficiency of the fuel processor, which was not optimized [22]. Pasel et al. proved that Jülich's ATR 14 fueled by diesel could produce H_2 and converse carbon from 99.70% to 99.98% [23]. Although these studies showed the feasibility of utilizing diesel reforming to fuel PEMFC, they focused on the reformer and did not analyze PEMFC system performances.

Some research groups have analyzed diesel-fueled PEMFC systems. Cutillo et al. conducted a simulation study based on ATR and SR processes to compare two different PEMFC 10 kW diesel processing systems, confirming that the SR system achieves a higher APU efficiency. However, they also noted that ATR's scheme is less complicated and has a better water balance than SR's [24]. Samsun et al. developed an integrated diesel fuel processing system for high-temperature proton-exchange membrane fuel cell (HT-PEMFC) [25–28]. The authors simulated a diesel-fueled HT-PEMFC system and calculated a system efficiency of 22.3% [25]. They also conducted an experimental study of a 28 kW fuel processor, which achieved fuel conversion higher than 99.95% and CO concentrations lower than 1% [28]. Pregelj et al. presented control strategies and electronic hardware solutions for diesel-powered fuel cell APUs. The solutions enable reliable and durable operation by controlling system-threatening phenomena, such as CO poisoning. They suggested the net efficiency of the system is 19.3% at 55% load and 18.4% at 85% load [29]. Malik et al. control the ATR temperature and hydrogen flow rate of diesel ATR for a 3.6 kW PEMFC system. By combining PI and PID controllers, they achieved fast response capabilities and almost no deviations [30].

Though these studies have proved the feasibility of diesel-fueled PEMFC systems, they have not explored the

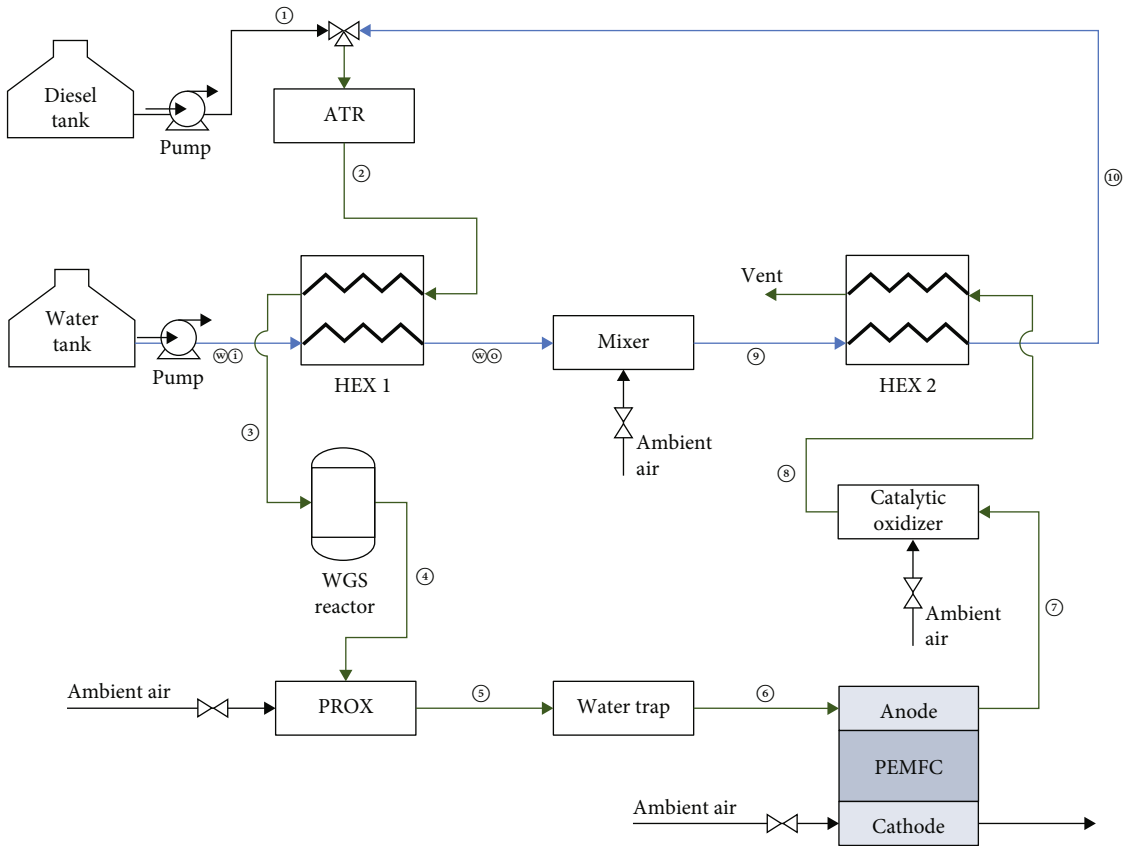

Figure 1: ATR-PEMFC system schematic.

optimal design and operating conditions of the system. In addition, they have not shown whether the proposed system is superior to the system using the hydrogen PEMFC system in the life-cycle GHG emissions point of view. To evaluate the significance of the proposed system, not only the system efficiency but also the quantitative comparison of the life-cycle GHG emissions with the alternative systems should be necessarily performed.

This paper is aimed at addressing this research gap. The main goals of the study are to determine the optimal design and operating condition of a diesel-powered ATR-PEMFC system and analyze the life-cycle GHG emissions of the system compared to those of a hydrogen-fueled PEMFC system. To achieve these goals, we conduct four types of analyses: assess overall system characteristics, conduct a parametric analysis to clarify control parameter effects, design an optimal system based on these results, and conduct a life cycle analysis (LCA) on our proposed system to evaluate the life-cycle GHG emissions based on system simulation results. We defined four main control parameters (heat exchanger effectiveness, steam-to-carbon ratio, oxygen-to-carbon ratio, and fuel utilization factor) and analyzed the system performance varying the value of the control parameters to determine the optimal design. In the life cycle analysis part, the proposed diesel-fueled PEMFC is compared with the H_2-fueled PEMFC in the life-cycle GHG emissions point of view, which is newly conducted in this study.

In Section 2, we describe our ATR-PEMFC system. In Section 3, the modelling of the system components using MATLAB and Cantera thermodynamic toolbox is introduced. PEMFC and system operational characteristics are analyzed in Section 4. In addition, a system operation parametric study is conducted to determine the design point of this operation. Based on Section 4's system simulation results, we also calculated and compared life-cycle greenhouse gas emissions of electricity generated from diesel-fueled PEMFC systems with hydrogen-fueled PEMFC in Section 5.

2. System Description

Figure 1 illustrates the ATR-PEMFC system schematic proposed in this study, consisting of a PEMFC, an ATR, and a balance of plant (BoP) components, which are connected and continuously affect one another. Room temperature and atmospheric pressure diesel and a steam and air mixture are inputs to the ATR. ATR outlet temperatures were maintained at 800°C and higher to ensure a complete reforming reaction, and outlet gas was cooled by heat exchange with water in the heat exchanger (HEX) 1. Preheated steam was then mixed with air in the mixer. The mixture of steam and air is heated again in the HEX 2 and fed with diesel into the ATR.

After the reformed gas has cooled in HEX 1, it passes through a WGS reactor to reach equilibrium at the reactor inlet temperature. The synthesis gas (syngas) obtained from

the WGS reactor contains a small amount of CO, which must be removed before entering the PEMFC because it requires high-purity H_2 with less than 10 ppm CO as fuel. To this end, PROX oxidizes the CO with air, increasing the outlet temperature. The outlet gas is cooled and condensed in a water trap at 80°C. The outlet gas is then supplied to the anode, whereas the air is sent to the PEMFC cathode. The PEMFC produces water (H_2O) and electric power by reacting H_2 with O_2. The remaining H_2 in the anode off-gas is completely combusted through a catalytic oxidizer with air. The catalytic oxidizer's outlet gas transfers heat in HEX 2 and exhausts through the vent.

3. Methods

Steady-state simulation models of the system components were constructed using MATLAB (MathWorks), the Cantera thermodynamic toolbox, and GRI 3.0 mechanisms. Specifically, a zero-dimensional (0D) model was designed for all system components to alleviate computational complexity. We then considered an electrochemical reaction model for the PEMFC. In addition to the thermodynamic gas states used in this system, the previously mentioned software also calculated thermodynamic equilibria and chemical reactions.

3.1. PEMFC. A single PEMFC stack comprises 60 serially connected cells, and the PEMFC comprises 25 stacks connected in parallel. An anode, membrane, cathode, fuel channel, and air channel compose each PEMFC cell.

Mass and energy conservation are considered in the model, and an electrochemical model was constructed. The utilization factor determined the amounts of fuel and air supplied to the PEMFC. Table 1 presents PEMFC simulation model equations with relevant references. The PEMFC model parameters are summarized in Table 2. Stack design, PEMFC cell size, and other geometric parameters were determined from the literature [31, 32].

The model is validated considering the reported results of three experiments [31], in which operating pressures varied from 1 to 3 atm with 70°C fuel cell and humidification temperatures on both the anode and cathode sides. All experimental conditions are summarized in Table 3, and the fitting parameters are listed in Table 4.

Figure 2 indicates that the simulation model was well-fitted with experimental results for all cases. This validation highlights that the PEMFC 0D model can reliably predict PEMFC operation in the general operating conditions considered in this study.

3.2. ATR. ATR reforms diesel with air and steam to produce syngas. $C_{12}H_{23}$ is the assumed diesel fuel chemical formula. The $C_{12}H_{23}$ lower heating value (LHV) is 43.1 MJ/kg, and the formation enthalpy is 305.35 kJ/mol [36]. The main reforming reactions in ATR are (1) total oxidation, (2) partial oxidation (POX), (3) steam reforming, and (4) the water-gas shift reaction.

$$C_nH_m + \left(n + \frac{m}{4}\right)O_2 \longrightarrow n\mathrm{CO}_2 + \frac{m}{2}\mathrm{H}_2\mathrm{O}, \quad (1)$$

$$C_nH_m + \left(\frac{n}{2} + \frac{m}{4}\right)O_2 \longrightarrow n\mathrm{CO} + \frac{m}{2}\mathrm{H}_2, \quad (2)$$

$$C_nH_m + n\mathrm{H}_2\mathrm{O} \longrightarrow n\mathrm{CO} + \left(n + \frac{m}{2}\right)\mathrm{H}_2, \quad (3)$$

$$\mathrm{CO} + \mathrm{H}_2\mathrm{O} \leftrightarrow \mathrm{CO}_2 + \mathrm{H}_2. \quad (4)$$

This study assumes the ATR model is adiabatic and all hydrocarbons in the gas are fully reformed at 800°C or higher. Thus, the minimum ATR outlet gas temperature is set as 800°C because hydrocarbons in the gas cannot be fully reformed when ATR's temperature(T_{ATR}) is lower than 800°C [21]. For simplicity, ATR outlet gases consist only of H_2, CO, CO_2, H_2O, and N_2. The outlet gas is also assumed to be in the equilibrium of the WGS reaction's equilibrium.

According to Moe [37], outlet gas composition is determined using the equilibrium constant (K_p) calculated using Eq. (5). Using the temperature-dependent equilibrium constant and partial-pressure-based definitions, an equilibrium relationship between CO, CO_2, H_2, and H_2O is obtainable. Based upon three reactions and the equilibrium relationship, an outlet gas mixture of ATR is predicted.

$$K_p = \exp\left(-4.33 + \frac{4577.8}{T(K)}\right) = \frac{P_{\mathrm{CO}_2} \bullet P_{\mathrm{H}_2}}{P_{\mathrm{CO}} \bullet P_{\mathrm{H}_2\mathrm{O}}}. \quad (5)$$

3.3. BoP

3.3.1. WGS Reactor. The WGS reactor increased the syngas H_2 fraction generated in the ATR by achieving WGS reaction equilibrium at lower temperatures. The WGS reactor is assumed to be isothermal, and outlet gas compositions were determined with Eq. (5).

A low-temperature WGS reactor typically operates at 180–250°C; at temperatures below 180°C, the catalytic activity becomes sluggish [38]. Therefore, the minimum WGS reactor temperature in this study is 180°C.

3.3.2. PROX. PROX preferentially oxidizes CO in the WGS reactor's outlet gas. We assumed that the CO is totally oxidized in the PROX, thus the gas before entering the PEMFC stack does not contain the CO, and it ensures no catalyst poisoning effect in the PEMFC. It is assumed that a stoichiometric air amount is supplied to PROX and that the process is adiabatic.

3.3.3. Water Trap. The water trap cools PROX outlet gas and removes water through condensation. When the water's partial pressure in the gas is higher than its saturation pressure at the operating temperature, the water is condensed and drained. If the water's partial pressure in the gas is lower than its saturation pressure, the gas is only cooled. The water trap outlet temperature is assumed to be equal to the operating temperature of PEMFC, i.e., 80°C.

3.3.4. Catalytic Oxidizer. The catalytic oxidizer oxidizes the remaining H_2 in the PEMFC outlet gas and is assumed to be adiabatic. Therefore, the air amount supplied to the catalytic oxidizer is determined as the stoichiometric amount.

Table 1: PEMFC simulation model equations.

Mass balances	$\dot{m}_{an,out} + \dot{m}_{ca,out} = \dot{m}_{an,in} + \dot{m}_{ca,in}$
Energy balances	$V \times i = \dot{m}_{an,in}h_{an,in} + \dot{m}_{ca,in}h_{ca,in} - \dot{m}_{an,out}h_{an,out} - \dot{m}_{ca,out}h_{ca,out} - Q_{PEMFC}$
Electrochemical reactions	PEMFC cell voltage $E = E_{oc} - E_{act} - E_{con} - E_{ohm}$ Nernst equation $E_{oc} = E_{rev} + (RT/2F)\ln\left[p_{H_2}\sqrt{p_{O_2}}\right]$ [33] $E_{rev} = E^o_{rev} + (T - T_{ref}) \times (\Delta S^o/nF)$ [33] Activation loss $E_{act} = E^{an}_{act} + E^{cat}_{act}$ [33] $E^{an}_{act} = (RT/\alpha_{an}F)\ln(j/j^{an}_0)$ [33] $E^{cat}_{act} = (RT/\alpha_{cat}F)\ln(j/j^{cat}_0)$ [33] $j_0 = \gamma_M \exp[-(\Delta G_C/R)(1/T - 1/T_{ref})]j^{ref}_0$ [33] Ohmic loss $E_{ohm} = R_{mem} \bullet I$ [33] $R_{mem} = \delta_{mem}/A\sigma_{mem}$ [33] $\sigma_{mem} = (0.005139\lambda - 0.00326)\exp[-(\Delta G/R)(1/T_{ref} - 1/T)]$ [33] Concentration loss $E_{con} = E^{an}_{con} + E^{cat}_{con} + E^{an}_{con,BV} + E^{cat}_{con,BV}$ [33] $E^{an}_{con} = (RT/nF)\ln(j^{an}_L/j^{an}_L - i)$ [34] $E^{cat}_{con} = (RT/nF)\ln\left(j^{cat}_L/j^{cat}_L - i\right)$ [34] $E^{an}_{con,BV} = (RT/\alpha_{an}F)\ln(j^{an}_L/j^{an}_L - i)$ [34] $E^{cat}_{con,BV} = (RT/\alpha_{cat}F)\ln(j^{cat}_L/j^{cat}_L - i)$ [34] $j^{an}_L = nFD^{an}_{eff}\left(C^{ch}_{H_2}/\delta^{an}_{el}\right)$ [34] $j^{cat}_L = nFD^{cat}_{eff}\left(C^{ch}_{O_2}/\delta^{cat}_{el}\right)$ [34] $C^{ch}_{H_2} = \frac{P_{an}X_{H_2,in}}{RT}$ $C^{ch}_{O_2} = \frac{P_{cat}X_{O_2,in}}{RT}$ $D^{an}_{eff} = (\varepsilon/\xi)\left(\left(1/D^{H_2-H_2O}_{eff}\right) + \left(1/D^{H_2O,K}_{eff}\right)\right)^{-1}$, $D^{cat}_{eff} = (\varepsilon/\xi)\left(\left(1/D^{O_2-H_2O}_{eff}\right) + \left(1/D^{H_2O,K}_{eff}\right)\right)^{-1}$ [34] $D^{i-H_2O}_{eff} = 0.0026T^{3/2}/pM_{i-H_2O}{}^{1/2}\sigma_{i,H2O}{}^2\Omega_{D,i-H_2O}$ [35] $M_{i-H_2O} = 2 \times ((1/M_i) + (1/M_{H2O}))^{-1}$ [35] $D^{H_2O,K}_{eff} = 2/3r\sqrt{8RT/\pi M_{H_2O}}$ [35] $\Omega_{D,i-H_2O} = \left(1.06/\tau_{i-H_2O}{}^{0.156}\right) + \left(0.193/\exp\left(0.476\tau_{i-H_2O}\right)\right) + \left(1.036/\exp\left(1.53\tau_{i-H_2O}\right)\right) + \left(1.765/3.894\tau_{i-H_2O}\right)$ [33]
Chemical reactions	Electrochemical reactions Fuel electrode (FE) $H_2 + O_2 \leftrightarrow H_2O + 2e^-$ Oxidant electrode (OE) $0.5O_2 + 2e^- \leftrightarrow O^{2-}$ Overall reactions $H_2 + 0.5O_2 \leftrightarrow H_2O$

3.3.5. HEX. The system contains HEX 1 and HEX 2, counter-flow HEXs. The HEX model is constructed using HEX effectiveness ($\eta_{effectiveness}$) to calculate the amount of heat transmitted from the hot side to the cold side. The HEXs are modeled using

$$Q_{max,h} = H_{h,i} - H_{h,o@T_{c,i}},\ Q_{max,c} = H_{c,o@T_{h,i}} - H_{c,i},\ Q_{max} = \min(Q_{max,h}, Q_{max,c}), \quad (6)$$

$$Q = Q_{max} \times \eta_{effectiveness}. \quad (7)$$

First, the maximum transferable heat amount is calculated using Eq. (6). $H_{h,i}$ denotes hot-side gas' inlet enthalpy, and $H_{h,o@T_{c,i}}$ denotes hot-side gas enthalpy when its temperature becomes the cold-side gas' inlet temperature. Similarly, $H_{c,o@T_{h,i}}$ denotes cold-side gas enthalpy when its temperature becomes the hot-side gas' inlet temperature. Q is the actual amount of heat transferred and is calculated using Q_{max} and $\eta_{effectiveness}$, as shown in Eq. (7) [39].

3.3.6. Mixer. The mixer combines the air and water required to reform diesel in the ATR and is assumed to be adiabatic. The outlet temperature and composition are determined based on mass and energy conservation.

3.3.7. Others. In addition to the abovementioned system components, the system includes pumps and valves. Pump energy consumption is assumed to be negligible because the working fluid is liquid, which does not require considerable energy. Moreover, the energy amount used in controlling the valves is also assumed to be negligible.

Table 2: PEMFC model parameters.

Parameter	Value
PEMFC geometry parameters	
A	$51.84\,cm^2 = (7.2\,cm \times 7.2\,cm)$ [31]
δ_{mem}	0.0108 cm [31]
δ_{el}	0.00129 cm [31]
δ_{GDL}	0.03 cm [31]
Electrochemical reaction parameters	
α_{an}	0.5 [31]
α_{ca}	2 [31]
ΔG_c^{an}	$29\,kJ\,mol^{-1}$ [32]
ΔG_c^{ca}	$66\,kJ\,mol^{-1}$ [32]
ρ_{H_2O}	$1\,g\,cm^{-3}$ [32]
ρ_{el}	$10.6 \times 10^{-6}\,\Omega\,cm$ [32]
ρ_p^{an}	$16.0 \times 10^{-3}\,\Omega\,cm$ [32]
ρ_p^{cat}	$43.1 \times 10^{-6}\,\Omega\,cm$ [32]
D_w	$1.28 \times 10^{-6}\,cm^2 s^{-1}$ [32]
ε	0.3 [32]
ξ	4 [32]

Table 3: PEMFC model validation conditions. [31].

	Case 1	Case 2	Case 3
Cell pressure (atm)	1	2	3
Cell temperature (°C)	70	70	70
Humidification temperature (°C)	70	70	70

Table 4: Fitted model parameters.

Parameter	Value
$i_{0,an}^{ref}$	$1 \times 10^{-5}\,A\,cm^{-2}$
$i_{0,ca}^{ref}$	$1 \times 10^{-9}\,A\,cm^{-2}$
γ_M	30
r_{pore}	2.5×10^{-6} m
μ_{fuel}	0.7
μ_{air}	0.5

4. Results

This study has four objectives. The first is to analyze operational ATR-PEMFC system component characteristics. Section 4.1 discusses component temperature, outlet gas composition, and flow rate in representative system operating conditions. PEMFC current density, voltage, power, and efficiency are also analyzed. Second, we conducted a parametric analysis to clarify how parameter variations influence system operation, as discussed in Sections 4.2.1–4.2.3. Sections 4.2.1#x2013;4.2.3 assess varying heat exchanger effectiveness ($\eta_{effectiveness}$), steam-to-carbon ratio (α_{SCR}) and oxygen-to-carbon ratio (α_{OCR}), and PEMFC fuel utilization factor (μ_{fuel}), respectively. Our third objective is to design an optimal system based on the parameter analysis results and evaluate its performance under the given conditions. As described in Section 4.2.4., the system operation design point is determined based on Sections 4.2.1–4.2.3 results. The fourth objective is to conduct a life cycle analysis on our proposed system, which is discussed in Section 5.

The parameters assumed for the system analysis are listed in Table 5, and the conditions are summarized in Table 6. The diesel flow rate is fixed as 0.015 mol/s, corresponding to PEMFC's~0.5 A/cm^2 current density and ~25 kW power at μ_{fuel} 0.7.

4.1. Component Operations in the ATR-PEMFC System. We selected a representative system operating condition ($\eta_{effectiveness}$ 0.7, α_{SCR} 2.5, α_{OCR} 0.6, and μ_{fuel} 0.7) to analyze operating characteristics. Table 7 presents each gas's temperature, pressure, mole fraction, molar flow rate, and mass flow rate.

The table shows that the ATR outlet gas (stream 2) temperature is 1018.5°C. The gas consists only of H_2, H_2O, CO, CO_2, O_2, and N_2 because complete reforming is assumed. Stream 2 passes through HEX 1 without a composition change and cools to 430.2°C.

Water at room temperature and atmospheric pressure is input into HEX 1, heated to 416.3°C, and mixed with the preheated stream (stream wo). Stream 9 is output with an increased flow rate, and the temperature is lowered to 227.3°C. Next, stream 9 is preheated to 485.7°C in HEX 2. Then outlet gas (stream 10) is mixed with Stream 1 and supplied to the ATR.

Stream 3 reaches equilibrium in the WGS reactor at the reactor's inlet temperature. H_2 and CO_2 flow rates increase, and H_2O and CO flow rates decrease while passing through the WGS reactor. In the referenced case, CO and H_2 flow rates after the WGS reactor are 0.0171 and 0.2994 mol/s, respectively.

Stream 4 and air are fed to the PROX to burn CO. PROX outlet gas (stream 5) temperature is 529.4°C, which is then cooled to 80°C in the water trap and output as stream 6.

To operate the PEMFC, stream 6 and ambient air are input into the anode and cathode, respectively. The H_2 flow rate in the anode outlet gas (stream 7) becomes lower than the anode inlet gas (stream 6) as PEMFC uses H_2 to generate electricity. In this case, PEMFC operates at a current density, voltage, and power of 0.5201 A/cm^2, 0.6624 V, and 26.79 kW, respectively. PEMFC power generation efficiency (η_{PEMFC}), the PEMFC power to the H_2 input ratio, is 37.00%. The system's overall efficiency (η_{system}), the PEMFC power to supplied diesel fuel ratio, is 24.81%.

To oxidize the remaining H_2 in the PEMFC outlet gas, stream 7 is channeled to the catalytic oxidizer. The catalytic oxidizer outlet gas (stream 8) has a temperature of 591.1°C and only consists of H_2O, CO_2, and N_2. Stream 8 cools to 401.0°C in HEX 2 and exits through the vent.

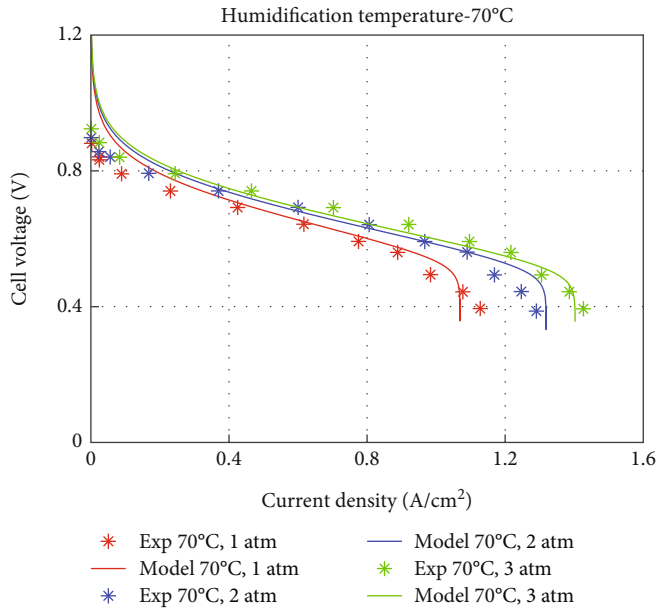

Figure 2: J–V curves at the validation conditions.

Table 5: Assumed system parameters.

Parameter	Value
Ambient temperature (T_1, T_{wi}, T_{air})	25°C
Stream condensation temperature	80°C
PEMFC operating temperature	80°C

In the system, unrecovered 18.87 kW, 24.81 kW, and 15.20 kW of heat were lost during the water trap's cooling and condensation, PEMFC power generation, and vent gases, respectively. Heat loss decreases system efficiency, so minimizing loss enhances system performance.

4.2. Parametric Study to Determine the System Operation Design Point

4.2.1. $\eta_{effectiveness}$ Variation. This section discusses how the $\eta_{\text{effectiveness}}$ variation from 0.7 to 0.85 influences system performance. Figure 3 shows the system operation results with different $\eta_{\text{effectiveness}}$.

ATR, WGS reactor, and PROX outlet gas temperatures with $\eta_{\text{effectiveness}}$ variation are shown in Figure 3(a). Increasing the HEX effectiveness means increasing the heat exchange rate between the HEX's two inlet streams. Because high $\eta_{\text{effectiveness}}$ in the system decreases the WGS inlet stream's temperature, the temperature of the WGS reactor and PROX decrease as well. In contrast, as $\eta_{\text{effectiveness}}$ increases, the HEX 1 cold-side outlet gas (stream wo)'s temperature increases, and the ATR inlet gas (stream 10)'s temperature also increases. This increases the ATR outlet gas temperature. Figure 3(b) shows H_2 and CO concentrations in the WGS reactor's outlet gas. As the WGS reaction is exothermic, lower temperature helps increasing H_2 concentration and lowering CO concentration. As shown in Figure 3(a), the WGS reactor's (stream 3) inlet temperatures decrease when $\eta_{\text{effectiveness}}$; this raises H_2 and lowers CO concentrations. Lower CO concentrations help reduce PROX outlet gas temperature, which is helpful to reduce relevant heat losses by reducing the oxidation of CO.

Figure 3(c) illustrates PEMFC current density and voltage. As the H_2 flow rate increased after the WGS reaction, the PEMFC current density increased as the fuel utilization factor is fixed at 0.7. Consequently, overvoltage increased, and cell voltage decreased. Combining these two trade-off effects, high $\eta_{\text{effectiveness}}$ increases the PEMFC driving fuel H_2 and generates more power (Figure 3(d)). Consequently, the system efficiency increases alongside $\eta_{\text{effectiveness}}$ (Figure 3(e)).

Significant system heat losses are noted in Figure 3(f). The heat loss in the water trap declines concurrently with the PROX outlet gas's temperature decline. In this case, the PROX outlet gas and 80°C (water-trap operating temperature) temperature differences decrease. PEMFC heat loss escalates as its current density escalates. As the H_2 flow rate in the PEMFC outlet gas rises, the catalytic oxidizer temperature also rises. Thus, the vent gas and room temperature difference increase, which makes heat loss from the vent slightly increase. The figure displays how overall heat losses were reduced because the water trap heat loss reduction was greater than the increase from the PEMFC and vent. Generally, high $\eta_{\text{effectiveness}}$ means that the thermal energy in the HEX inlet streams is well utilized, which improves the system performance. Notably, the HEX maximum effectiveness is limited to 0.85 for typical engineering practice. Based on these results, $\eta_{\text{effectiveness}}$ was fixed to 0.85 to improve system performance.

4.2.2. α_{SCR} and α_{OCR} Variations. α_{SCR} and α_{OCR} are key control parameters determining the system's inlet gas water vapor and O_2 flow rates, respectively. In this section, α_{SCR}

Table 6: System analysis conditions for each subsection.

Control parameters	4.1.	4.2.1.	4.2.2.	4.2.3.
Diesel fuel flow rate (mol/s)	0.015	0.015	0.015	0.015
$\eta_{effectiveness}$ (HEX 1, 2 effectiveness)	0.7	Variable	0.85	0.85
α_{SCR} (steam-to-carbon ratio)	2.5	2.5	Variable	2.5
α_{OCR} (oxygen-to-carbon ratio)	0.6	0.6	Variable	0.6
μ_{fuel} (fuel utilization factor of the PEMFC)	0.7	0.7	0.7	Variable
μ_{air} (air utilization factor of the PEMFC)	0.5	0.5	0.5	0.5
P_{system} (system pressure, atm)	1	1	1	1

Table 7: Each stream's temperature, pressure, molar compositions, mole flow rate, and mass flow rate.

	Temperature (°C)	Pressure (atm)	Molar compositions (%)	Mole flow rate (mol/s)	Mass flow rate (g/s)
Stream 1	25.0	1	$C_{12}H_{23}$ 100%	0.015	2.505
Stream 2	1018.5	1	H_2 18.10%, H_2O 33.4%, CO 8.1%, CO_2 6.8%, N_2 33.6%	1.209	25.45
Stream 3	430.2	1	H_2 18.10%, H_2O 33.4%, CO 8.1%, CO_2 6.8%, N_2 33.6%	1.209	25.45
Stream 4	430.2	1	H_2 24.8%, H_2O 26.7%, CO 1.4%, CO_2 13.5%, N_2 33.6%	1.209	25.45
Stream 5	529.4	1	H_2 24.1%, H_2O 26.0%, CO_2 14.5%, N_2 35.3%	1.241	26.62
Stream 6	80.0	1	H_2 24.1%, H_2O 26.0%, CO_2 14.5%, N_2 35.3%	1.241	26.62
Stream 7	80.0	1	H_2 8.7%, H_2O 31.3%, CO_2 17.4%, N_2 42.5%	1.031	26.20
Stream 8	591.1	1	H_2O 34.4%, CO_2 15.0%, N_2 50.6%	1.200	32.67
Vent	401.0	1	H_2O 34.4%, CO_2 15.0%, N_2 50.6%	1.200	32.67
Stream wi	25.0	1	H_2O 100%	0.45	8.11
Stream wo	416.3	1	H_2O 100%	0.45	8.11
Stream 9	227.3	1	H_2O 46.7%, O_2 11.2%, N_2 42.1%	0.964	22.94
Stream 10	485.7	1	H_2O 46.7%, O_2 11.2%, N_2 42.1%	0.964	22.94

varies from 0.5 to 3, and α_{OCR} varies from 0.4 to 0.7. The resulting influence on system performance was examined.

High α_{SCR} increases the H_2O mole flow rate in the ATR inlet gas. As α_{SCR} increases, T_{ATR} decreases because the endothermic SR reaction becomes more favorable as the H_2O amount increases (Figure 4(a)). As the water flow rate increases, heat transferred from the ATR outlet gas to water also increases; thus, WGS reactor inlet gas temperatures decrease.

Because of the lower WGS reactor temperature, the H_2 mole flow rate rises and CO mole flow rate lowers, which also lowers the PROX outlet gas temperature (Figure 4(b)).

Figures 5(a)–5(d) show PEMFC current density, voltage, power, and system efficiency. When α_{SCR} increases, the H_2 mole flow rate increases after the WGS reaction, increasing current density and decreasing cell voltage. High α_{SCR} mainly helps promoting the reforming reaction and increases the H_2 production, which is required for PEMFC power generation. Therefore, PEMFC power and efficiency increase as α_{SCR} increases.

High α_{OCR} increases the O_2 mole flow rate in the ATR inlet gas. In the ATR, oxygen's higher mole flow rate increases exothermic oxidation reactions. It accelerates POX reaction and prevents WGS reaction by increasing the reactor's temperature. Therefore, the higher the α_{OCR}, the higher the T_{ATR} (Figure 4(a)). Furthermore, as α_{OCR} increases, inlet gas temperatures to the WGS reactor increase, and thus, the H_2 mole flow rate lowers and the CO mole flow rate rises. Thus, the PROX outlet gas temperatures and water-trap heat loss increase (Figure 4(b)).

As shown in Figure 5, as α_{OCR} increases, the PEMFC fuel H_2 flow rate decreases, decreasing current density and overvoltage and increasing cell voltage. Combining these effects, PEMFC power and efficiency decrease when α_{OCR} increases.

Figures 5(e)–5(h) show major system heat losses with different α_{SCR} and α_{OCR}. As α_{SCR} rises and α_{OCR} lowers, water-trap heat loss is reduced by decreasing the PROX outlet gas temperature. PEMFC heat loss intensifies because its current density increases as the fuel cell reaction is the exothermic reaction. Vent gas heat loss increases because the H_2 mole flow rate in Stream 7 and the catalytic oxidizer outlet gas temperatures increase. Thus, vent gas heat loss reaches the maximum at a certain α_{SCR} and decreases after the peak because the H_2O mole flow and the HEX 2 exchanged heat rates increase. Overall, the system heat loss decreases as α_{SCR} increases and α_{OCR} decreases.

As shown in Figure 4(a), when α_{OCR} is 0.4 and α_{SCR} is 0.5, 1, and 3, T_{ATR} is lower than 800°C (the minimum ATR outlet gas temperature). Thus, these are unsuitable operating conditions.

When α_{SCR} is greater than a certain value, the H_2O mole flow rate increases, and the H_2 mole flow rate does not

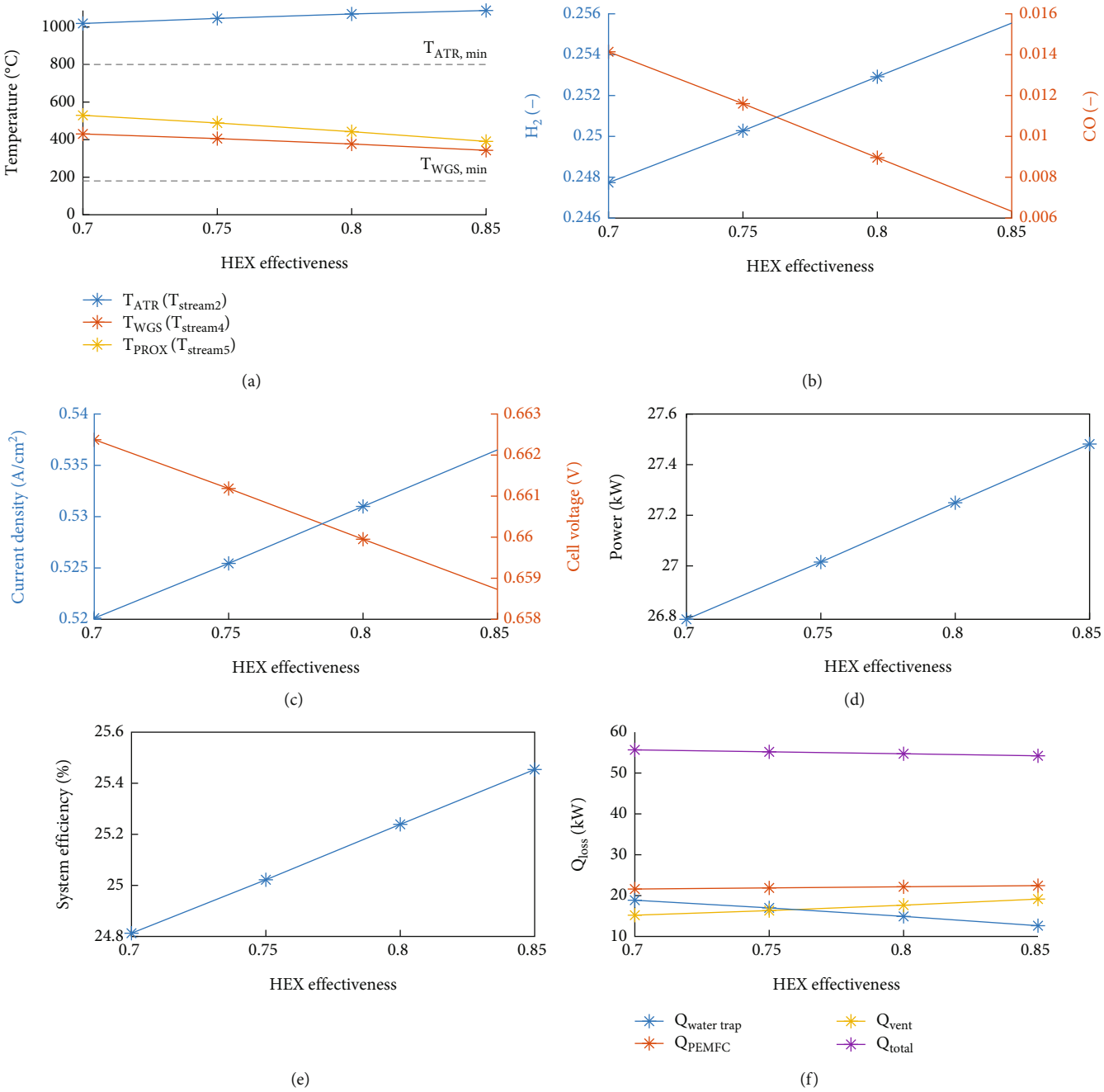

FIGURE 3: ATR-PEMFC system performance with $\eta_{effectiveness}$ variation: (a) temperatures; (b) mole fraction after the WGS reactor; (c) current density and cell voltage; (d) power; (e) system efficiency; and (f) heat losses.

increase. This is because the diesel's mole flow rate is fixed in the system. Therefore, when α_{SCR} is set to be greater than 2, the amount of H_2 in the stream does not notably increase, and the system efficiency cannot be significantly improved.

4.2.3. μ_{fuel} Variations. μ_{fuel} is a control parameter directly affecting PEMFC current density and power generation for a given system's fuel supply. This section examines μ_{fuel} influence by varying μ_{fuel} from 0.7 to 0.95.

Figure 6 shows system operation results from varying μ_{fuel}. Figure 6(a) shows the ATR, WGS reactor, and PROX outlet gas temperature. As μ_{fuel} increases, the H_2 flow rate in the anode off-gas (stream 7) decreases, the catalytic oxidizer outlet temperature decreases, and the HEX 2 cold-side outlet gas temperature (stream 10) decreases. Therefore, ATR, WGS reactor, and PROX outlet gas temperatures decrease overall.

When the WGS reaction occurs at a lower temperature with increasing μ_{fuel}, the H_2 concentration increases and the CO concentration decreases (Figure 6(b)). When μ_{fuel} is greater than 0.85, ATR outlet gas and WGS reactor temperatures decreased, and the H_2 mole fraction in the PEMFC inlet gas does not increase significantly.

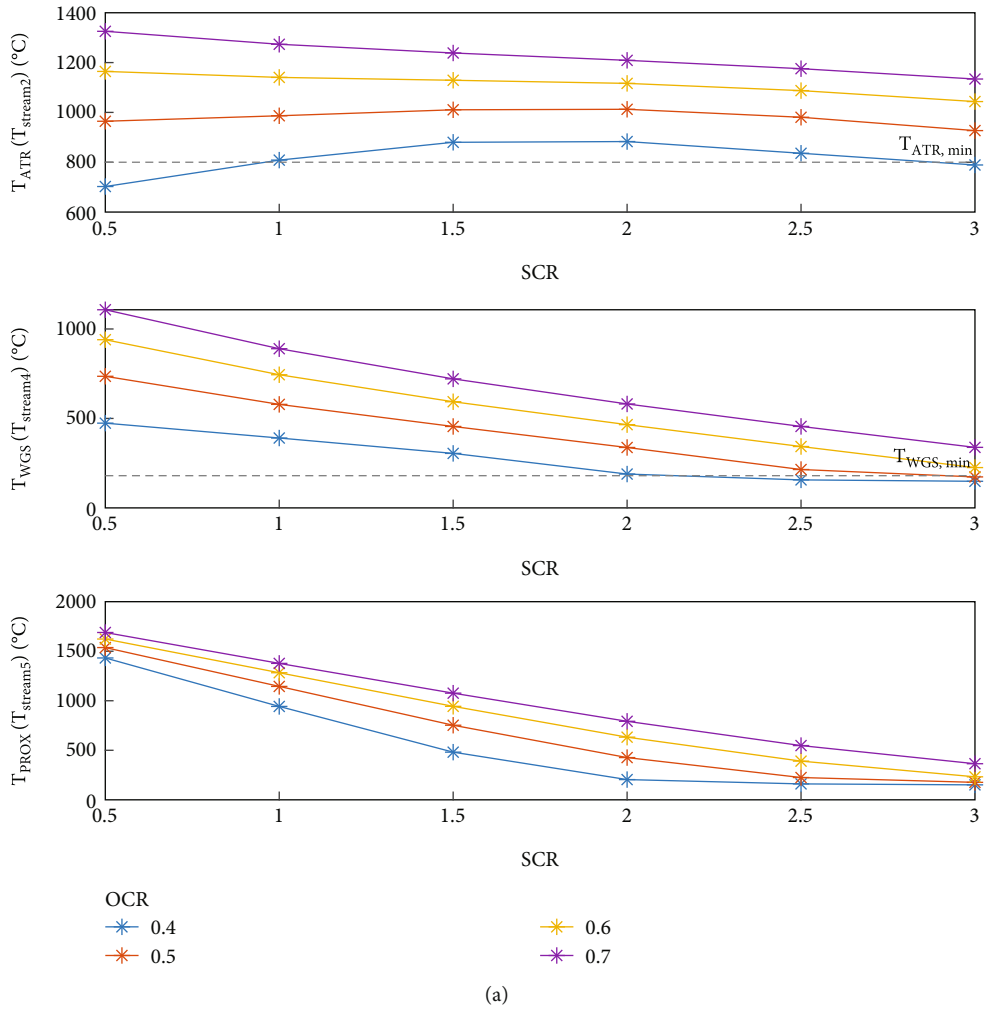

(a)

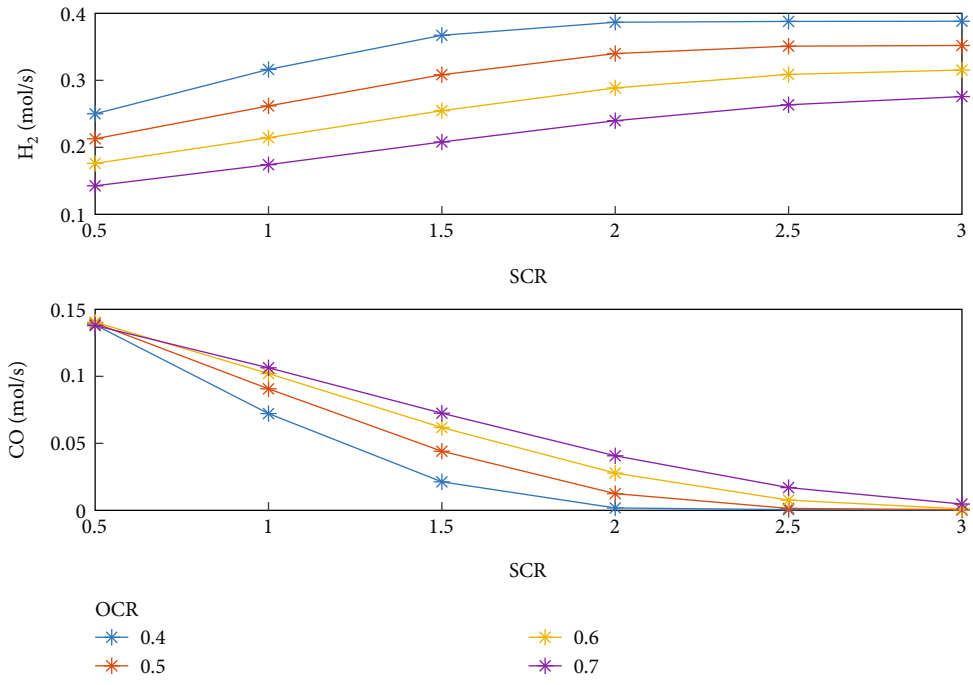

(b)

Figure 4: Stream characteristics with α_{SCR} and α_{OCR} variation: (a) temperatures and (b) mole flow rate after the WGS reactor.

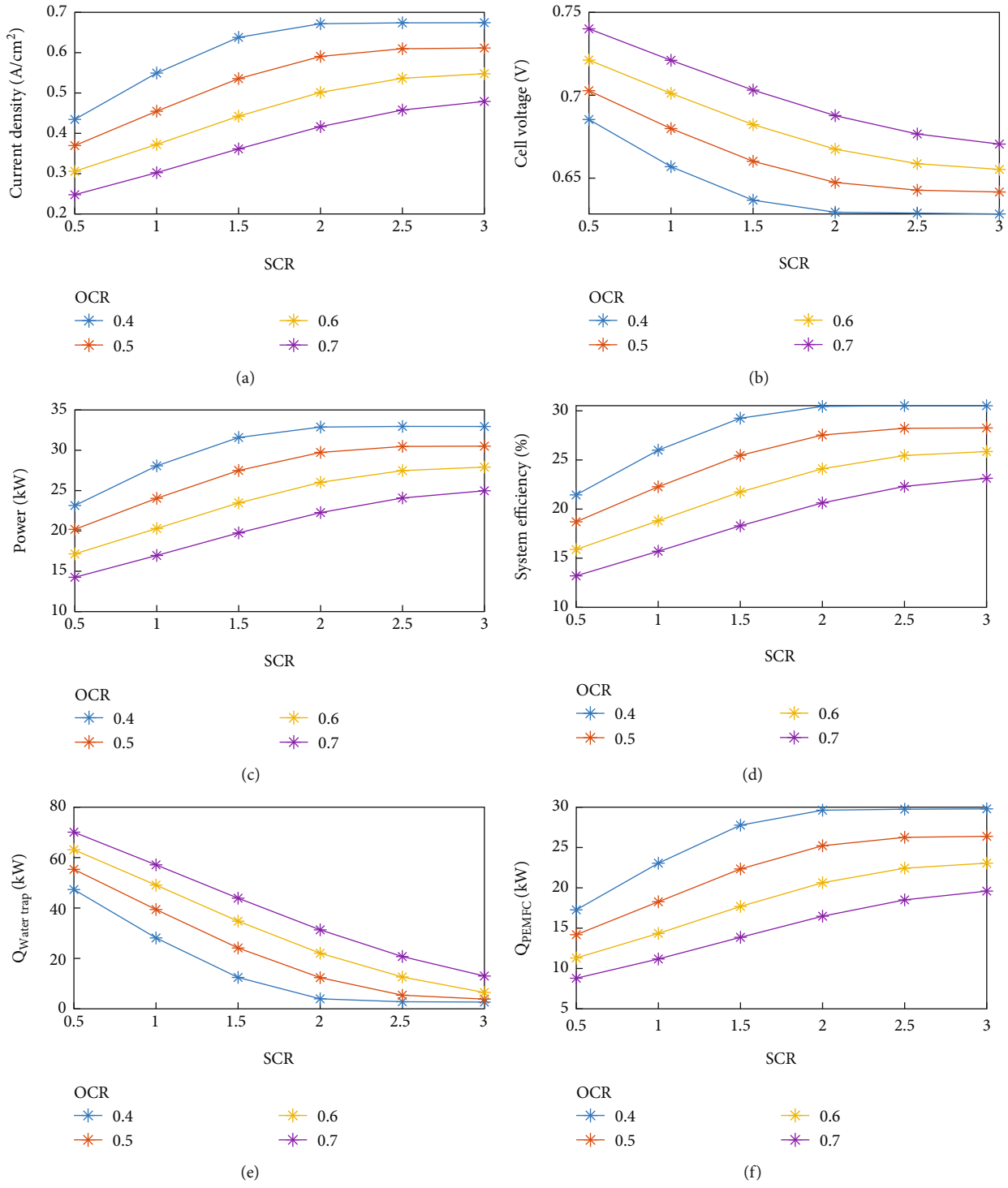

Figure 5: Continued.

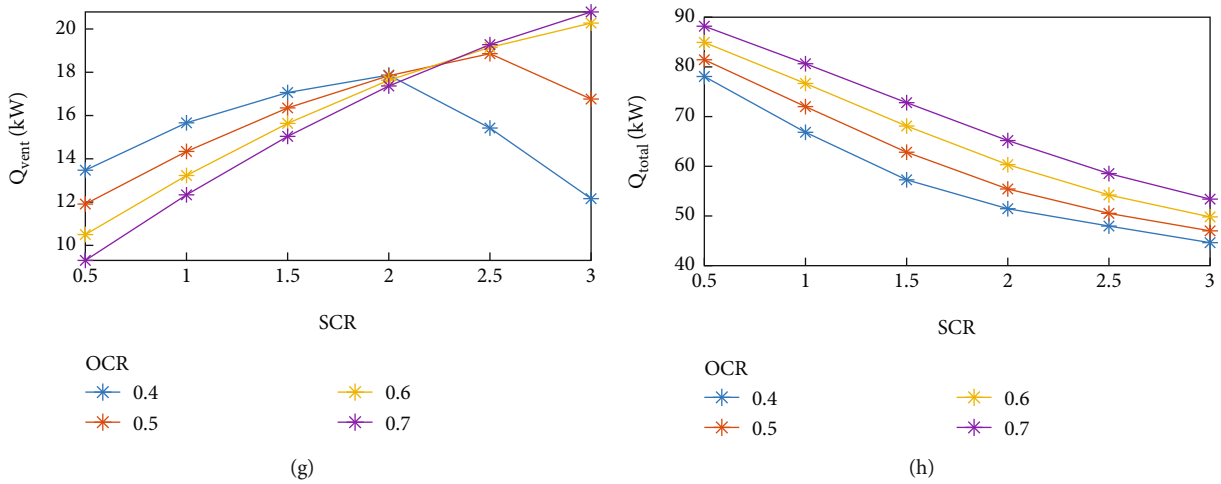

FIGURE 5: ATR-PEMFC system performance with α_{SCR} and α_{OCR} variation: (a) current density; (b) cell voltage; (c) power; (d) system efficiency; (e) heat loss in water trap; (f) heat loss in PEMFC; (g) heat loss in vent; and (h) total heat loss.

High μ_{fuel} mainly means that PEMFC utilizes hydrogen well. As the diesel mole flow rate is fixed, the current density increases with increasing the fuel cell reaction. The cell voltage decreases as the current density increases (Figure 6(c)). PEMFC power increases overall because the current density increase is greater than the decreasing voltage (Figure 6(d)). Figure 6(e) shows how the system efficiency increases alongside μ_{fuel}. However, considering the PEMFC performance, there is an upper limit to the applicable fuel utilization factor.

Figure 6(f) shows the significant system heat losses with increased μ_{fuel}. When the PROX outlet gas temperature decreases, water trap heat loss also decreases. In addition, PEMFC heat loss intensifies because the current density increases and the exothermic fuel cell reaction. By increasing μ_{fuel}, the H_2 molar flow rate in the anode off-gas, catalytic oxidizer temperature, and vent gas heat loss decrease. Since water trap and vent heat loss reduction is greater than PEMFC's heat loss increase, the overall heat loss reduces as μ_{fuel} increases.

4.2.4. System Operation Results at the Design Point. Sections 4.2.1–4.2.3 results determined the system design point as $\eta_{effectiveness}$ 0.85, α_{SCR} 2, α_{OCR} 0.5, and η_{fuel} 0.85. System performance and minimum-temperature ATR and WGS reactor conditions were considered when establishing the design point.

Table 8 presents system operation results at the design point. The PEMFC produces 34.91 kW of power, and system efficiency is 32.25% at the design point. Table 9 presents every gas's temperatures, pressures, mole fraction, molar flow rate, and mass flow rate at the design point.

4.3. System with Anode Off-Gas Recirculation. This section determines whether anode off-gas recirculation effects can improve performance. By implementing anode off-gas recirculation, the H_2 remaining in the anode off-gas can be used as fuel for PEMFC power generation, thus, reducing the heat loss from H_2 oxidation in the catalytic oxidizer. Figure 7 schematically illustrates this updated system. Because the recirculation ratio typically varies from 0.4 to 0.8 [40], we set the recirculation ratio as 0.4 in this study.

Table 10 organizes the operating system results. When anode off-gas is added to the system, the temperature of the catalytic oxidizer outlet gas (stream 8) temperature decreases because the H_2 mole flow rate in the catalytic oxidizer inlet gas decreases. Therefore, vent gas heat loss decreases.

In addition, because stream 8's temperature decreases and less heat is exchanged in HEX 2, steam 10's temperature decreases. Thus, the stream temperatures decrease overall as they pass through the system, and water trap heat loss also decreases.

However, the PEMFC current density increases due to anode off-gas recirculation, which increases the overvoltage and decreases the cell voltage. Therefore, PEMFC heat loss increases.

Although anode off-gas recirculation can increase the power generation to 35.73 kW and system efficiency to 33.09% through the more efficient use of fuel, the minimum ATR and WGS reactor temperature (800°C, 180°C) conditions cannot be satisfied by decreasing stream temperatures.

Figure 8 illustrates an alternative system with anode off-gas recirculation. In this framework, the HEX 2 location is changed to achieve the minimum-temperature condition by exchanging the catalytic oxidizer outlet gas and ambient air to reduce vent heat loss and increase stream 10's temperature.

Table 11 presents the system's operational characteristics shown in Figure 8. Compared with Table 10, ATR outlet, WGS inlet, and PROX outlet gas temperatures increase, and the minimum temperature condition is satisfied.

However, because the WGS driving temperature is higher, the H_2 mole flow rate in the PEMFC inlet stream is reduced, and the PEMFC power and system efficiency are slightly lower than those in Table 10. As a result, PEMFC power is 35.62 kW, and the system efficiency is 33.00%. Furthermore, the recirculation ratio can be set higher than 0.4 in

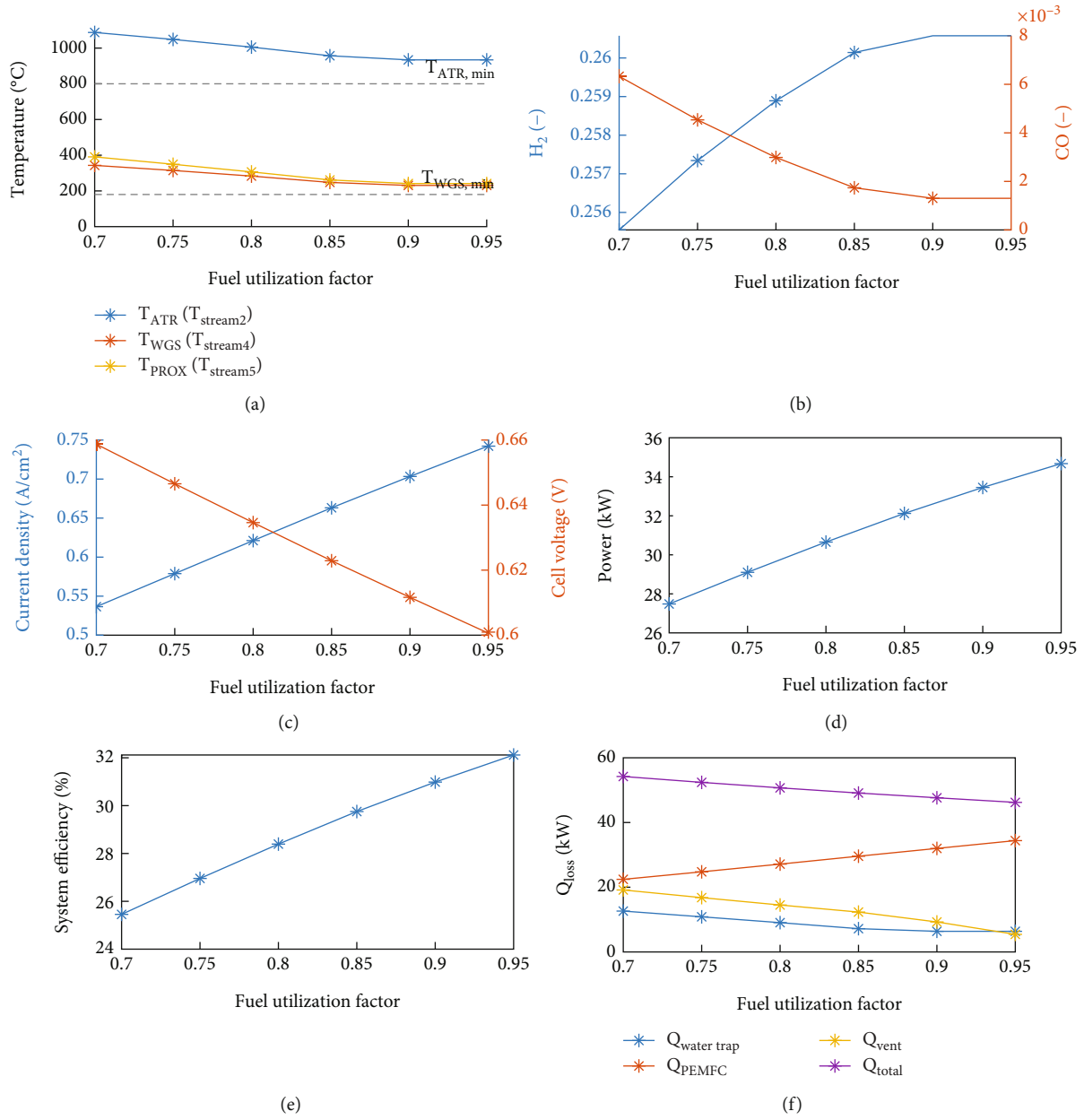

FIGURE 6: ATR-PEMFC system performance with μ_{fuel} variation: (a) temperatures; (b) mole fraction after the WGS reactor; (c) current density and cell voltage; (d) power; (e) system efficiency; and (f) heat losses.

this system because stream temperatures are higher than the minimum temperature condition.

However, if the recirculation ratio is set to 0.6, the PEMFC current density is greater than 0.8 A/cm^2 and the cell voltage decreases to 0.562 V. Therefore, PEMFC power and the system efficiency are lower to 35.54 kW and 32.92%, respectively.

In summary, when the system operates at the design point determined in Section 4.2.4, system efficiency improves by less than 1% from recirculating anode off-gas. Thus, system efficiency did not noticeably improve.

As shown in Table 11, PEMFC had the highest heat losses, which means decreasing heat losses and increasing performance can only be achieved with a better PEMFC. It should be noted that efficiency over 40% is achievable when the system has a more efficient PEMFC.

5. Life Cycle Analysis

In this section, life-cycle greenhouse gas emissions of electricity generated from our proposed system at a construction site are evaluated and compared with a hydrogen-fueled PEMFC generator utilizing an off-site hydrogen production site. It is assumed that a large natural gas reforming plant produces and compresses hydrogen and transports it to the construction site with a tube trailer.

Table 8: System operation results at the design point.

Operating conditions		Performance	
Control parameters		*PEMFC*	
$\eta_{effectiveness}$ (HEX 1, 2 effectiveness)	0.85	Average cell current density	0.7374 A/cm^2
α_{SCR} (Steam-to-carbon ratio)	2.0	Cell voltage	0.6073 V
α_{OCR} (Oxygen-to-carbon ratio)	0.5	PEMFC power	34.82 kW
μ_{fuel} (Fuel utilization factor of PEMFC)	0.85	PEMFC efficiency	41.19%
μ_{air} (Air utilization factor of PEMFC)	0.5	*Heat losses (kW)*	
P_{system} (System pressure)	1 atm	Water trap	5.934
Temperatures (°C)		PEMFC	33.79
ATR outlet (stream 2)	866	Vent	9.967
WGS outlet (stream 4)	230.4	Total heat loss	49.69
PROX outlet (stream 5)	252.7	*Efficiency*	
Water trap outlet (stream 6)	80	Total system efficiency	32.25%
Anode outlet (stream 7)	80		

Table 9: Each stream's temperature, pressure, molar composition, mole flow rate, and mass flow rate at the design point.

	Temperature (°C)	Pressure (atm)	Molar compositions (%)	Mole flow rate (mol/s)	Mass flow rate (g/s)
Stream 1	25	1	$C_{12}H_{23}$ 100%	0.015	2.505
Stream 2	868	1	H_2 24.05%, H_2O 26.62%, CO 9.49%, CO_2 7.6%, N_2 32.2%	1.051	21.35
Stream 3	230.4	1	H_2 24.1%, H_2O 26.6%, CO 9.5%, CO_2 7.6%, N_2 32.2%	1.051	21.35
Stream 4	230.4	1	H_2 33.27%, H_2O 17.40%, CO 0.28%, CO_2 16.9%, N_2 32.2%	1.051	21.35
Stream 5	252.7	1	H_2 33.1%, H_2O 17.3%, CO_2 17.0%, N_2 32.6%	1.056	21.55
Stream 6	80	1	H_2 33.1%, H_2O 17.3%, CO_2 17.0%, N_2 32.6%	1.056	21.55
Stream 7	80	1	H_2 6.9%, H_2O 24.1%, CO_2 23.7%, N_2 45.3%	0.759	20.95
Stream 8	496.8	1	H_2O 27.4%, CO_2 21.0%, N_2 51.6%	0.858	24.56
Vent	367.2	1	H_2O 27.4%, CO_2 21.0%, N_2 51.6%	0.858	24.56
Stream wi	25	1	H_2O 100%	0.36	6.49
Stream wo	592.1	1	H_2O 100%	0.36	6.49
Stream 9	317.7	1	H_2O 45.7%, O_2 11.4%, N_2 42.9%	0.789	18.85
Stream 10	470.5	1	H_2O 45.7%, O_2 11.4%, N_2 42.9%	0.789	18.85

The GREET program developed by the Argonne National Laboratory in the United States was used for life cycle analysis (LCA). The life-cycle GHG emissions of natural gas, electricity, and diesel in the U.S. were calculated through GREET 2021 (Table 12). It is important to note that the analysis of GHG emissions generated during the hydrogen charging station construction or fuel cell product production is beyond the scope of this paper.

The life cycle of the diesel-fueled PEMFC system consists of crude oil production, diesel production, diesel transportation, and PEMFC operation (Figure 9). The GHG emissions generated from those processes are from the U.S. default values of GREET 2021 [41]. We note that it is assumed that large diesel-fueled trucks transport diesel.

The diesel-fueled PEMFC system efficiency is already calculated in Table 8. The diesel-fueled PEMFC system efficiency was calculated as 32.25%.

The life cycle of an H_2-fueled PEMFC system consists of natural gas production, steam methane reforming process, H_2 compression, H_2 transportation, and PEMFC operation (Figure 9). It is necessary to determine reforming process efficiencies to calculate GHG emissions generated from natural gas reforming. This study used large off-site reforming plant efficiencies from the H2A model of the National Renewable Energy Laboratory in the United States. Specifically, a 71.9% efficiency [42] was used.

Hydrogen is compressed from 10 bar to 200 bar pressure to be loaded on a tube trailer and transported to a construction site. The tube trailer is assumed to supply hydrogen to the PEMFC generator at the construction site.

The power consumed in compressing gaseous hydrogen was calculated based on the work per unit mass consumed in reversible adiabatic gas compression, as expressed in Eq. (7), an equation derived from thermodynamics. $Z(= Pv/RT)$

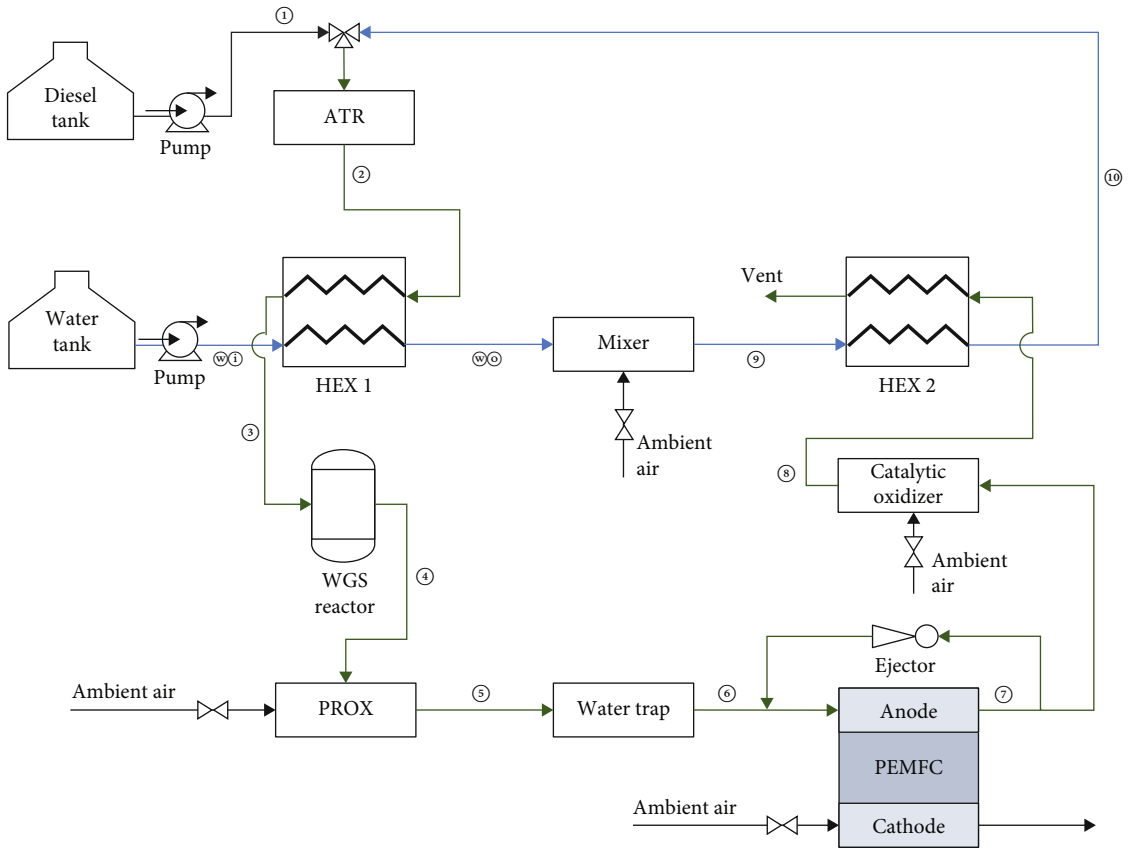

Figure 7: ATR-PEMFC system schematic with anode off-gas recirculation.

Table 10: System operation characteristics with anode off-gas recirculation.

Operating conditions		Performance	
Control parameters		*Heat losses (kW)*	
$x_{\text{recirculation}}$ (ratio of anode off-gas recirculation)	0.4	Water trap	3.764
Temperatures (°C)		PEMFC	37.64
ATR outlet (stream 2)	799.0	Vent	7.474
WGS inlet (stream 3)	179.2	Total heat loss	48.88
PROX outlet (stream 5)	187.6	*Efficiency*	
PEMFC		Total system efficiency	33.09%
Cell voltage	0.5827 V		
PEMFC power	35.73 kW		
PEMFC efficiency	39.52%		

denotes a compressibility factor, which considers differences from the ideal gas when the gas is at high pressure.

$$\begin{aligned} w &= -\int_1^2 P dv = -\int_1^2 \frac{C}{v^{\gamma}} dv = \frac{C}{\gamma - 1}\left[{v_2}^{1-\gamma} - {v_1}^{1-\gamma}\right] \\ &= \frac{1}{\gamma - 1}\left[P_2 v_2 - P_1 v_1\right] = \frac{1}{\gamma - 1} P_1 v_1 \left[\frac{P_2 v_2}{P_1 v_1} - 1\right] \\ &= \frac{1}{\gamma - 1} P_1 v_1 \left[{P_{\text{ratio}}}^{\gamma - 1/\gamma} - 1\right] \\ &= Z \times RT \times \frac{1}{\gamma - 1}\left[{P_{\text{ratio}}}^{\gamma - 1/\gamma} - 1\right]. \end{aligned} \tag{8}$$

Since hydrogen compression involves a large compression ratio, compression and cooling are repeatedly conducted to increase efficiency. According to GREET 2021, compression work per unit mass consumed can be calculated with Eq. (9) [41]. N_s indicates by how many steps the compression was divided.

$$w = Z \times RT \times \frac{1}{2} \times N_s \times \frac{\gamma}{\gamma - 1}\left[{P_{\text{ratio}}}^{\gamma - 1/N_s \gamma} - 1\right]. \tag{9}$$

The isentropic efficiency was set to 80% when

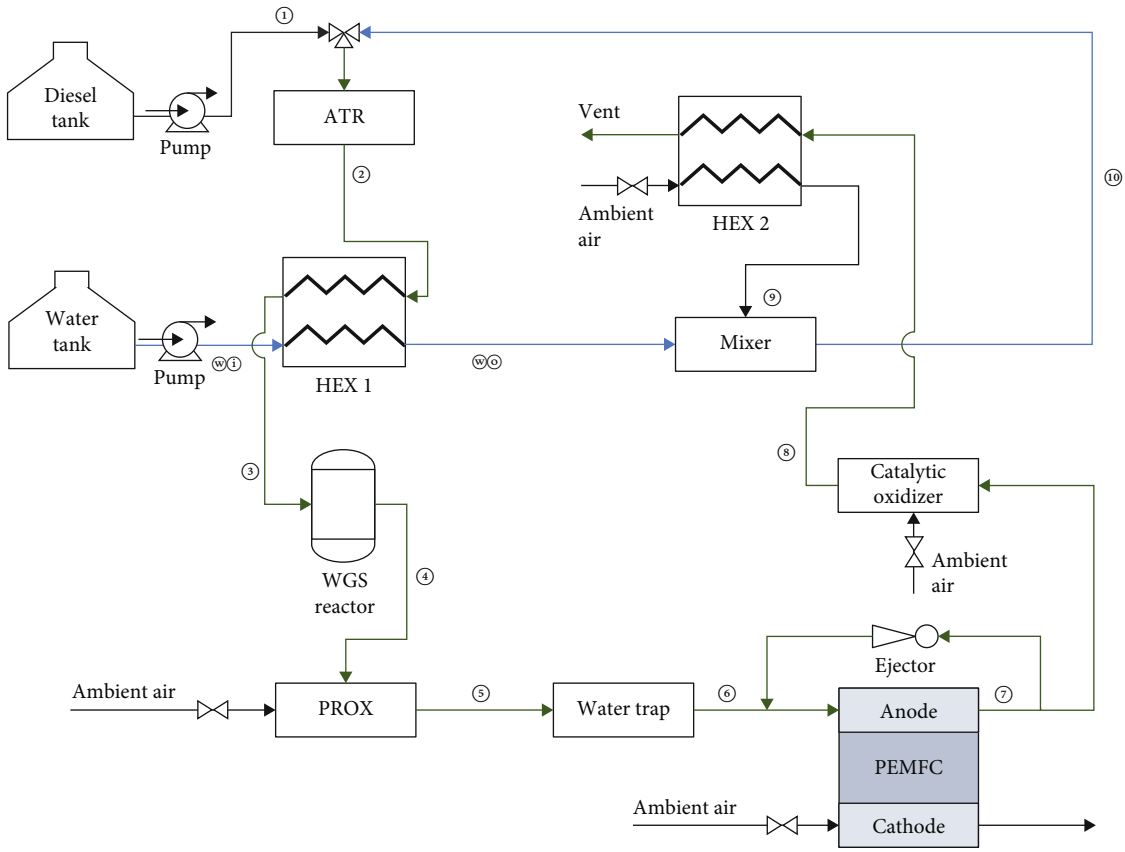

Figure 8: Improved ATR-PEMFC system schematic with anode off-gas recirculation.

Table 11: Improved system operation characteristics with anode off-gas recirculation.

Operating conditions		Performance	
Control parameters		*Heat losses (kW)*	
$x_{recirculation}$ (ratio of anode off-gas recirculation)	0.4	Water trap	5.573
Temperatures (°C)		PEMFC	37.45
ATR outlet (Stream 2)	858.0	Vent	5.675
WGS inlet (Stream 3)	222.9	Total heat loss	48.70
PROX outlet (Stream 5)	243.5	*Efficiency*	
PEMFC		Total system efficiency	33.00%
Cell voltage	0.5833 V		
PEMFC power	35.62 kW		
PEMFC efficiency	39.57%		

Table 12: The life-cycle greenhouse gas emissions of natural gas, diesel, and electricity [41].

Life-cycle greenhouse gas emissions	CO_2 (g-CO_2/GJ)	CH_4 (g-CH_4/GJ)	N_2O (g-N_2O/GJ)	Total (g-CO_2-eq./GJ)
Natural gas	62,165	206.1	2.06	68,892
Diesel	87,228	105.0	0.58	90,531
Electricity	114,038	250.8	2.27	122,165

compressed from 10 to 200 bar. The compressibility factor (Z) was calculated for application according to each pressure range. Additionally, electric motor efficiency was set at 92%. All these parameters were referenced from GREET 2021 [41]. The hydrogen inlet temperature is assumed as 25°C. The compression work per unit mass consumed for loading hydrogen onto a tube trailer was calculated as 1.63 kWh/kg-H_2 (Table 13).

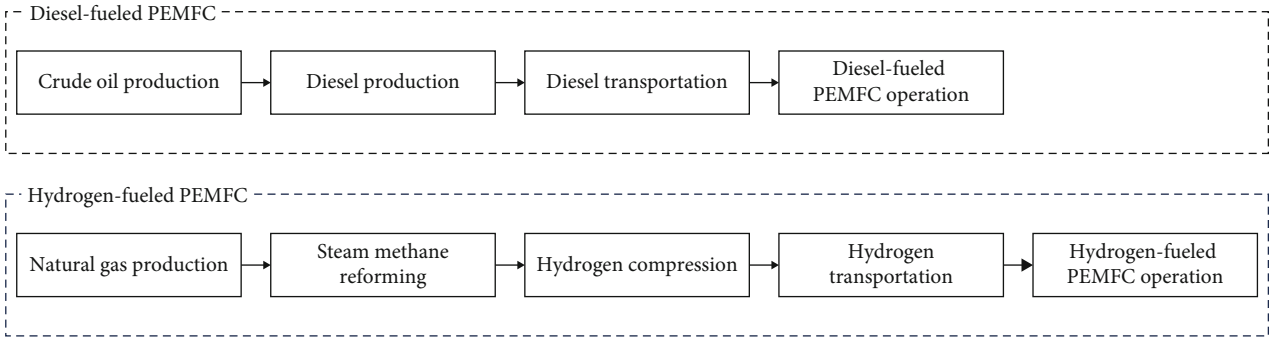

Figure 9: The life cycle of diesel-fueled PEMFC and hydrogen-fueled PEMFC systems.

Table 13: Work consumed for hydrogen compression.

	Tube trailer
Inlet pressure (bar)	10
Outlet pressure (bar)	200
Isentropic efficiency (%)	80%
Compressibility factor (Z)	1.07
Efficiency of electric motor (%)	92%
Theoretical work (kWh/kg)	1.21
Actual shaft work (kWh/kg)	1.51
Consumed electrical energy (kWh/kg)	1.63

A tube trailer transports 250 kg of hydrogen. In this study, it is assumed that large diesel-fueled trucks transport hydrogen. According to GREET 2021, the fuel economy is assumed to be 7.2 miles/diesel gallon when hydrogen is loaded and 9.0 miles/diesel gallon when hydrogen is not loaded [41]. 36 MJ/l was used for U.S. conventional diesel heating values referenced from GREET 2021 [41]. The energy required to transport the unit mass of gaseous hydrogen is summarized in Table 14. Determining the distance from the hydrogen production site to the hydrogen charging site is necessary for off-site hydrogen production. However, it is difficult to accurately obtain this distance because the hydrogen production plant location has not yet been determined. Therefore, the transportation distance is assumed to be 300 km (Figure 10), and then analyze the effect relative to transportation distance (Figure 11). In this study, we assumed that the transportation distance of hydrogen and that of diesel is the same.

The hydrogen-fueled PEMFC system efficiency must be determined to calculate emissions from hydrogen-fueled PEMFC operation. The electrical efficiency of PEMFs is generally between 40 and 60% [43]. Giddey et al. suggested that the electrical efficiency of the PEMFC stack varied from 39 to 41% [44]. Omran et al. showed that the overall PEMFC system efficiency was 47.5% at around 50% of the rated power [45]. Chen et al. developed a 30 kW vehicle PEMFC system model and achieved the maximum electrical efficiency of 41% [46]. Wang et al. suggested that the PEMFC efficiency can reach as high as 65% [47].

In this study, the hydrogen-fueled PEMFC system efficiency was also calculated for the simulation model. The hydrogen-fueled PEMFC system generated the same power as the diesel-fueled PEMFC system at the design point (34.82 kW, as determined in Section 4.2.4). PEMFC system efficiency was calculated as 43.13%, which is feasible compared to the literature, when hydrogen is used as fuel. The operating conditions and results of the PEMFC system fueled by hydrogen are summarized in Table 15.

Figure 10 compares the life-cycle GHG emissions of electricity generated from diesel-fueled and H_2-fueled PEMFC systems with a 300 km transportation distance. The figure shows the GHG emissions by each process. We note that the efficiency of each process is utilized in the LCA, and the uncertainties in the efficiencies of processes are also considered in the analysis; it is assumed that the energy use of each process can be varied by 10%.

The total GHG emissions of diesel-fueled PEMFC were 1010.2 g-$CO_{2\text{-eq}}$/kWh, which was very similar to that of H_2-fueled PEMFC (1001.1 g-$CO_{2\text{-eq}}$/kWh). For the case of a diesel-fueled PEMFC system, the largest portion of GHG emissions were generated from using diesel in the system to produce electricity. In the case of H_2-fueled PEMFC, however, the largest portion of GHG emissions was generated from steam methane reforming; there are no GHG emissions from the electricity generation process because it uses hydrogen as fuel. As shown in the figure, during the production process, diesel emits more GHG emissions than natural gas. This is, because, generally crude oil needs a more sophisticated process to make diesel than raw natural gas does to become natural gas. It is also noted that the CO_2 emissions per heating value of diesel is greater than that of natural gas.

Notably, the GHG emissions from H_2 transportation are considerable, whereas diesel transportation emits lower GHG emissions, though the diesel transportation distance and the hydrogen transportation distance are assumed to be the same. The main reason for this result is that the volumetric energy density of H_2 is much smaller than that of diesel. Thus, if the distance to transport hydrogen is long, using diesel can be more environmentally friendly.

Electrical life-cycle GHG emissions from a hydrogen-fueled PEMFC system are calculated relative to transportation distance (Figure 11). The life-cycle GHG emissions of electricity generated by the diesel-fueled PEMFC system

Table 14: Transportation energy consumption.

	Gaseous hydrogen transportation
From hydrogen producer to hydrogen charging station (when hydrogen is loaded)	0.0470 MJ/km/kg-H_2
From hydrogen charging station to hydrogen producer (when hydrogen is not loaded)	0.0373 MJ/km/kg-H_2
Total	0.0843 MJ/km/kg-H_2

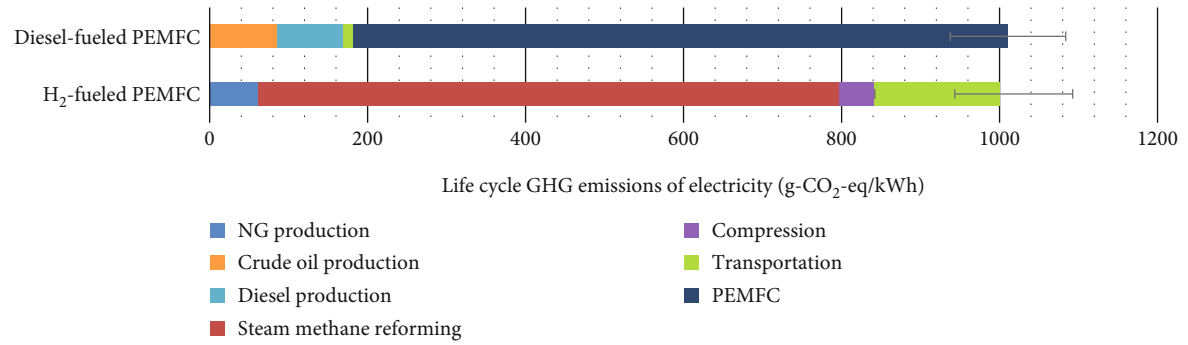

Figure 10: The life-cycle GHG emissions of electricity generated from PEMFC systems with a 300 km transportation distance.

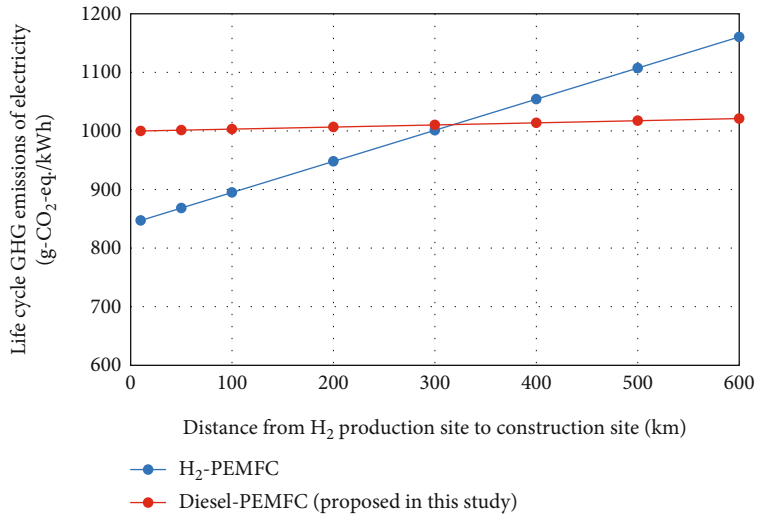

Figure 11: The life cycle GHG emissions of electricity generated from PEMFC systems relative to transportation distance.

Table 15: PEMFC system fueled by hydrogen operating condition and results.

Operating conditions		Performance	
Control parameters		*PEMFC*	
$\eta_{effectiveness}$ (HEX 1, 2 effectiveness)	0.85	Average cell current density	0.7045 A/cm^2
μ_{fuel} (Fuel utilization factor of PEMFC)	0.85	Cell voltage	0.6360 V
μ_{air} (Air utilization factor of PEMFC)	0.5	PEMFC power	34.82 kW
P_{system} (System pressure)	1 atm	PEMFC efficiency	43.13%
$\dot{m}_{H_2}$ (mole flow rate of hydrogen)	0.334 mol/s		

are slightly varied relative to transportation distance. On the other hand, the electricity generated by the hydrogen-fueled PEMFC system varied considerably (Figure 10). When the distance from the hydrogen production site to the hydrogen charging site is less than 318 km, PEMFC power generation using reformed hydrogen expressed lower life-cycle GHG emission levels. However, with more than a 318 km distance, diesel-fueled PEMFC generates lower life-cycle GHG emissions than electricity generated by hydrogen-fueled PEMFC. Therefore, for a construction site far from the hydrogen

production plant, using a diesel-fueled PEMFC system is preferred from a life-cycle GHG emissions point of view.

6. Conclusions

Our research objectives are (1) to analyze the diesel-powered ATR-PEMFC system characteristics, (2) to clarify how each control parameter influences system operations, (3) to determine optimal operating conditions for high performance and stable operation and evaluate system performance at the design point, and (4) to evaluate life cycle GHG emissions from the proposed system. To this end, we analyzed simulation models constructed through MATLAB and the Cantera thermodynamic toolbox. In addition, GREET software, developed by the U.S. Argonne National Laboratory was utilized for life cycle analysis.

First, we schemed the diesel-powered ATR-PEMFC system and analyzed the system under the representative system operating conditions. Diesel is fully reformed in the ATR at high temperatures (~1018.5°C). The WGS and PROX are applied to remove CO and increase H_2 in PEMFC's inlet stream. The overall system efficiency was 24.81% in the reference case, which needs to be improved by system optimization.

Secondly, we assessed our system by varying control parameters. The ATR minimum operating temperature is set to 800°C [21] and the WGS minimum operating temperature is set to 180°C [38], which are necessary conditions for proper system operation. A high $\eta_{\text{effectiveness}}$) improved the system performance by reducing the WGS reactor's temperature and CO concentration. A high α_{SCR} enhanced system performance by favoring endothermic steam reforming reactions and increasing PEMFC inlet gas H_2 concentration. A low α_{OCR} enhances system performance by weakening the exothermic oxidation reaction and lowering the H_2 fraction in PEMFC inlet gas. However, there is an upper limit of α_{SCR} and a lower limit of α_{OCR} to meet the minimum temperature conditions. When μ_{fuel} increases, system efficiency increases by utilizing the H_2 fuel more efficiently.

Considering our parametric analysis results and the reactor's minimum temperature conditions, we determined optimal system operating conditions($\eta_{\text{effectiveness}}$ 0.85, α_{SCR} 2.0, α_{OCR} 0.5, and μ_{fuel} 0.85). At the optimal operating condition, we achieved a 32.25% efficiency and met the ATR and WGS's minimum temperature conditions. In addition, we suggested the system design with anode off-gas recirculation and improved the system efficiency by 33.00% at the same design point.

Lastly, the life-cycle GHG emissions of electricity generated from the proposed system were compared with a hydrogen-fueled PEMFC system. For the case of the U.S., the proposed system emits 1010.2 g-CO2-eq/kWh of greenhouse gas, and the hydrogen-fueled PEMFC system emits 1001.1 g-CO2-eq/kWh at a 300 km fuel transportation distance. We confirmed that the transportation's greenhouse gas emissions of diesel and that of hydrogen are considerably different at the same distance. Thus, transportation distance is key for diesel-fueled PEMFC to be more meaningful in a GHG emissions perspective than H_2-fueled PEMFC. This study suggests that, with a transportation distance greater than 318 km, the diesel-fueled PEMFC system emitted lower life-cycle GHG emissions than the hydrogen-fueled PEMFC system. Therefore, our proposed system is suitable for a construction site far from a hydrogen production location.

Notably, this study comprehensively characterizes the diesel-fueled PEMFC system operation. The study also conducted life cycle analysis, unlike previous studies, to analyze GHG emissions of diesel-fueled PEMFC. We demonstrated the usefulness of diesel-fueled PEMFC at construction sites by determining the transportation distances that diesel-fueled PEMFC was environmentally advantageous. Our findings can promote future research, such as experimental demonstration or design optimization for system development. When conducting the empirical study, we can operate the system in the operating points that we determined in this study. In addition, hydrogen transportation costs a lot of money, but diesel transportation could be economical [48]. Therefore, techno-economic analysis is required for future research to quantitatively analyze the economic feasibility. The system efficiency and the operating points can be also used in technoeconomic analysis.

Nomenclature

A:	Active area of MEA
r:	Pore diameter for anode and cathode
P, p:	Pressure
$P_{\text{atm}}, p_{\text{atm}}$:	Atmospheric pressure
T:	Temperature
T_{atm}:	Atmospheric temperature
R:	Gas constant (8.3145 J/mol·K)
n:	Number of electrons
F:	Faraday constant (96,485 C/mol)
E:	Cell voltage
E^0_{rev}:	Standard state reversible voltage
E_{rev}:	Reversible voltage
E_{oc}:	Open-circuit cell voltage
E_{act}:	Activation overpotential
E_{ohm}:	Ohmic overpotential
E_{con}:	Concentration overpotential
$E_{\text{con,BV}}$:	Butler–Volmer overpotential
G:	Gibbs free energy
S:	Entropy
V:	Voltage
I, i:	Current
i_0:	Exchange current density
i_L:	Limiting current density
j:	Current density
j_0:	Exchange current density
R_{mem}:	Electrical resistance of membrane
M:	Molecular weight
$\dot{m}$:	Mass flow rate
k:	Thermal conductivity
K_p:	Equilibrium constant
Z:	Compressibility factor
D_w:	Diffusion coefficient
D^{i-k}_{eff}:	Binary diffusion coefficient

D^K_{eff}: Knudsen diffusion coefficient
D_{eff}: Effective diffusion coefficient
C: Molar concentration
H: Enthalpy (extensive)
h: Enthalpy (intensive)
Q: Heat transfer.

Greek Letters

γ_M: Roughness factor
λ: Humidification
δ: Thickness
σ: Conductivity
ε: Porosity
ξ: Tortuosity
$\Omega_{D,i-k}$: Dimensionless diffusion collision integral
τ_{i-k}: Lennard–Jones distance of species
σ_{i-k}: Mean molecular radii of species
α_{an}: Charge transfer coefficient for anode
α_{ca}: Charge transfer coefficient for cathode
μ: Utilization factor of PEMFC
ρ: Density
$\eta_{\text{effectiveness}}$: Heat exchanger effectiveness
η_{blower}: Blower efficiency
α_{SCR}: Steam-to-carbon ratio
α_{OCR}: Oxygen-to-carbon ratio.

Abbreviations

PEMFC: Proton-exchange membrane fuel cell
ATR: Autothermal reformer
GHG: Greenhouse gas
NOx: Nitrogen oxides
SOx: Sulfur oxides
PM: Particulate matter
HC: Hydrocarbon
MEA: Membrane electrode assembly
APUs: Auxiliary power unit
HT-PEMFC: High temperature proton-exchange membrane fuel cell
SR: Steam reforming
SMR: Steam methane reforming
BoP: Balance of plants
PROX: Preferential oxidizer
WGS: Water-gas shift
HEX: Heat exchanger
Syngas: Synthesis gas
FE: Fuel electrode
OE: Oxidant electrode
LHV: Lower heating value
POX: Partial oxidation
LCA: Life cycle analysis.

Superscripts and Subscripts

an: Anode
ca: Cathode
el: Electrolyte
ch: Channel
mem: Membrane
act: Activation loss
ohm: Ohmic loss
conc: Concentration loss
H_2: Hydrogen
O_2: Oxygen
CO: Carbon monoxide
CO_2: Carbon dioxide
H_2O: Water/steam
CH_4: Methane
N_2: Nitrogen
h: Hot side
c: Cold side
i: Inlet
o: Outlet
ref: Reference case.

Data Availability

All the figures are accessible to all readers. The data and figures are included in the article.

Conflicts of Interest

The authors declare that they have no conflicts of interest.

Acknowledgments

This work was supported by the Ewha Womans University Research Grant of 2022 and the Basic Science Research Program through the National Research Foundation of Korea (NRF) funded by the Ministry of Education (2021R1F1A1063229). This research has been performed as Project Open Innovation R&D (OTSK_2022_027) and supported by K-water.

References

[1] European Union, "Commission Delegated Regulation (EU) 2017/655 of 19 December 2016 supplementing Regulation (EU) 2016/1628 of the European Parliament and of the Council with regard to monitoring of gaseous pollutant emissions from in-service internal combustion engines installed in non-road mobile machinery," *Official Journal of the European Union*, pp. 3–26, 2017.

[2] United States, "Nonroad Diesel Engines. DieselNet," https://dieselnet.com/standards/us/nonroad.php.

[3] CARB developing tier 5 emission standards for off-road engines, "DieselNet," https://dieselnet.com/news/2021/11carb.php; 2021.

[4] Industry-Academic Cooperation Foundation of Chonnam National University, "Introduction of the new standard of domestic construction and agricultural equipments. Ministry of Environment," https://www.codil.or.kr/filebank/original/RK/OTKCRK200657/OTKCRK200657.pdf?stream=T; 2018.

[5] N. Yilmaz, F. M. Vigil, A. Atmanli, and B. Donaldson, "Influence of fuel oxygenation on regulated pollutants and unregulated aromatic compounds with biodiesel and n-pentanol blends," *International Journal of Energy Research*, vol. 2023, 11 pages, 2023.

[6] Noise and Vibration Control Act, "Act No. 17843," https://www.law.go.kr/%EB%B2%95%EB%A0%B9/%EC%86%8C%

EC%9D%8C%C2%B7%EC%A7%84%EB%8F%99%EA%B4%80%EB%A6%AC%EB%B2%95; 2021.

[7] Y. Oh, "Analysis of 3,819 cases of environmental disputes... account for 85% of noise and vibration damage. Ministry of Environment," http://me.go.kr/home/web/board/read.do;jsessionid=pfdCeIGQOJ18L9p3ETYZrAzC.mehome1?pagerOffset=1080&maxPageItems=10&maxIndexPages=10&searchKey=&searchValue=&menuId=&orgCd=&boardId=836090&boardMasterId=1&boardCategoryId=39&decorator=;2018.

[8] A. Kumar and M. Sehgal, "Hydrogen fuel cell technology for a sustainable future: a review," SAE Technical Paper, 2018.

[9] O. Z. Sharaf and M. F. Orhan, "An overview of fuel cell technology: fundamentals and applications," *Renewable and Sustainable Energy Reviews*, vol. 32, pp. 810–853, 2014.

[10] T. Taner, "Alternative energy of the future: a technical note of PEM fuel cell water management," *Journal of Fundamentals of Renewable Energy and Applications*, vol. 5, no. 3, pp. 1–4, 2015.

[11] F. Sun, D. Su, and Y. Yin, "A streamline dot flow field design for proton exchange membrane fuel cell," *International Journal of Energy Research*, vol. 2023, 12 pages, 2023.

[12] N. Atasay, A. Atmanli, and N. Yilmaz, "Liquid cooling flow field design and thermal analysis of proton exchange membrane fuel cells for space applications," *International Journal of Energy Research*, vol. 2023, 16 pages, 2023.

[13] Hydrogen Fuel Cell Generators for Construction, "FuelCellsWorks," https://fuelcellsworks.com/news/hydrogen-fuel-cell-generators-for-construction/;19 December 2022.

[14] GEH2, "The zero-emission hydrogen power generator. EODev," https://www.eo-dev.com/products/geh2-the-zero-emission-hydrogen-power-generator;.

[15] Construction world first, "GeoPura," https://www.geopura.com/in-action/construction-world-first/;.

[16] Case Study, "GeoPura Hydrogen Fuel Cell Module Mark 1. GeoPura, Simens Energy," https://documentcloud.adobe.com/link/review?uri=urn:aaid:scds:US:ddcc5ccd-9dd8-4b10-9ac2-70a94132f022.

[17] F. Rosa, E. López, Y. Briceño et al., "Design of a diesel reformer coupled to a PEMFC," *Catalysis Today*, vol. 116, no. 3, pp. 324–333, 2006.

[18] S. Krummrich, B. Tuinstra, G. Kraaij, J. Roes, and H. Olgun, "Diesel fuel processing for fuel cells–DESIRE," *Journal of Power Sources*, vol. 160, no. 1, pp. 500–504, 2006.

[19] B. Lindström, J. A. Karlsson, P. Ekdunge et al., "Diesel fuel reformer for automotive fuel cell applications," *International Journal of Hydrogen Energy*, vol. 34, no. 8, pp. 3367–3381, 2009.

[20] Y. Song, K. Han, and D. Wang, "Thermodynamic analysis of fossil fuels reforming for fuel cell application," *International Journal of Hydrogen Energy*, vol. 45, no. 39, pp. 20232–20239, 2020.

[21] D. Ješić, V. E. Zajec, D. Bajec, G. Dolanc, G. Berčič, and B. Likozar, "Computational investigation of auto-thermal reforming process of diesel for production of hydrogen for PEM fuel cell applications," *International Journal of Energy Research*, vol. 46, no. 12, pp. 17068–17083, 2022.

[22] K. Lee, G. Han, S. Cho, and J. Bae, "Pressurized diesel fuel processing using hydrogen peroxide for the fuel cell power unit in low-oxygen environments," *Journal of Power Sources*, vol. 380, pp. 37–45, 2018.

[23] J. Pasel, R. C. Samsun, J. Meißner, A. Tschauder, and R. Peters, "Recent advances in diesel autothermal reformer design," *International Journal of Hydrogen Energy*, vol. 45, no. 3, pp. 2279–2288, 2020.

[24] A. Cutillo, S. Specchia, M. Antonini, G. Saracco, and V. Specchia, "Diesel fuel processor for PEM fuel cells: two possible alternatives (ATR versus SR)," *Journal of Power Sources*, vol. 154, no. 2, pp. 379–385, 2006.

[25] R. C. Samsun, J. Pasel, R. Peters, and D. Stolten, "Fuel cell systems with reforming of petroleum-based and synthetic-based diesel and kerosene fuels for APU applications," *International Journal of Hydrogen Energy*, vol. 40, no. 19, pp. 6405–6421, 2015.

[26] R. C. Samsun, D. Krekel, J. Pasel, M. Prawitz, R. Peters, and D. Stolten, "A diesel fuel processor for fuel-cell-based auxiliary power unit applications," *Journal of Power Sources*, vol. 355, pp. 44–52, 2017.

[27] R. C. Samsun, M. Prawitz, A. Tschauder et al., "An integrated diesel fuel processing system with thermal start-up for fuel cells," *Applied Energy*, vol. 226, pp. 145–159, 2018.

[28] R. C. Samsun, M. Prawitz, A. Tschauder, J. Meißner, J. Pasel, and R. Peters, "Reforming of diesel and jet fuel for fuel cells on a systems level: Steady- state and transient operation," *Applied Energy*, vol. 279, p. 115882, 2020.

[29] B. Pregelj, A. Debenjak, G. Dolanc, and J. Petrovčič, "A diesel-powered fuel cell APU—reliability issues and mitigation approaches," *IEEE Transactions on Industrial Electronics*, vol. 64, no. 8, pp. 6660–6670, 2017.

[30] F. R. Malik, Z. Tieqing, and Y. B. Kim, "Temperature and hydrogen flow rate controls of diesel autothermal reformer for 3.6 kW PEM fuel cell system with autoignition delay time analysis," *International Journal of Hydrogen Energy*, vol. 45, no. 53, pp. 29345–29355, 2020.

[31] L. Wang, A. Husar, T. Zhou, and H. Liu, "A parametric study of PEM fuel cell performances," *International Journal of Hydrogen Energy*, vol. 28, no. 11, pp. 1263–1272, 2003.

[32] Z. Abdin, C. J. Webb, and E. M. Gray, "PEM fuel cell model and simulation in MATLAB-Simulink based on physical parameters," *Energy*, vol. 116, pp. 1131–1144, 2016.

[33] O. Ryan, C. Suk-Won, C. Whitney, and B. P. Fritz, *Fuel Cell Fundamentals (3rd ed.)*, Wiley, 2016.

[34] E. Hernández-Pacheco, D. Singh, P. N. Hutton, N. Patel, and M. D. Mann, "A macro-level model for determining the performance characteristics of solid oxide fuel cells," *Journal of Power Sources*, vol. 138, no. 1-2, pp. 174–186, 2004.

[35] E. Nagy, *Basic Equations of Mass Transport through a Membrane Layer (2nd Edition)*, Elsevier, 2019.

[36] Joint Research Centre, Institute for Energy and Transport, H. Maas, H. Hass, and A. Huss, "Well-to-wheels analysis of future automotive fuels and powertrains in the European context: tank-to-wheels report (TTW). Version 4a," Publications Office, 2014, https://data.europa.eu/doi/10.2790/95839.

[37] J. M. Moe, "Design of water-gas shift reactors," *Chemical Engineering Progress*, vol. 58, pp. 33–36, 1962.

[38] R. Fabian, R. Ashok, and S. Scott, "Water gas shift reactor modelling and new dimensionless number for thermal management/design of isothermal reactors," *Applied Thermal Engineering*, vol. 173, article 115033, 2020.

[39] W. Choi, J. Kim, Y. Kim, and H. H. Song, "Solid oxide fuel cell operation in a solid oxide fuel cell-internal combustion engine hybrid system and the design point performance of the hybrid system," *Applied Energy*, vol. 254, p. 113681, 2019.

[40] E. J. Choi, S. Yu, and S. M. Lee, "Optimization of operating conditions of a solid oxide fuel cell system with anode off-gas recirculation using the model-based sensitivity analysis," *Energies*, vol. 15, no. 2, p. 644, 2022.

[41] GREET, *2021 model*, U.S. Argonne National Laboratory, 2021, https://greet.es.anl.gov/greet_excel_model.models.

[42] H2A, "Hydrogen Analysis Productino Models-Current Central Hydrogen Production from Steam Methane Reforming of Natural Gas without CO2 Capture and Sequestration, U.S. NREL," 2018, https://www.nrel.gov/hydrogen/assets/docs/current-central-steam-methane-reforming-without-co2-sequestration-v3-2018.xlsm.

[43] S. Mekhilef, R. Saidur, and A. Safari, "Comparative study of different fuel cell technologies," *Renewable and Sustainable Energy Reviews*, vol. 16, no. 1, pp. 981–989, 2012.

[44] S. Giddey, F. T. Ciacchi, and S. P. S. Badwal, "Design, assembly and operation of polymer electrolyte membrane fuel cell stacks to 1 kW_e capacity," *Journal of Power Sources*, vol. 125, no. 2, pp. 155–165, 2004.

[45] A. Omran, A. Lucchesi, D. Smith et al., "Mathematical model of a proton-exchange membrane (PEM) fuel cell," *International Journal of Thermofluids.*, vol. 11, p. 100110, 2021.

[46] X. Chen, S. Long, L. He et al., "Performance evaluation on thermodynamics-economy-environment of PEMFC vehicle power system under dynamic condition," *Energy Conversion and Management*, vol. 269, article 116082, 2022.

[47] Y. Wang, Y. Pang, H. Xu, A. Martinez, and K. S. Chen, "PEM fuel cell and electrolysis cell technologies and hydrogen infrastructure development–a review," *Energy and Environmental Science*, vol. 15, no. 6, pp. 2288–2328, 2022.

[48] S. Singh, S. Jain, P. S. Venkateswaran et al., "Hydrogen: a sustainable fuel for future of the transport sector," *Renewable and Sustainable Energy Reviews*, vol. 51, pp. 623–633, 2015.